International Journal of Bifurcation and Chaos, Vol. 26, No. 2 (2016) 1650028 (22 pages)

DOI: 10.1142/S0218127416500280

Codimension-Two Bifurcation Analysis in DC Microgrids Under Droop Control

Eduardo Lenz* and Daniel J. Pagano†
Department of Automation and Systems,
Federal University of Santa Catarina,
Florianópolis, Brazil
**eduardo.lenz@posgrad.ufsc.br*
†*daniel.pagano@ufsc.br*

André P. N. Tahim
Department of Electrical Engineering,
Federal University of Bahia, Brazil
atahim@ufba.br

Received March 6, 2015; Revised September 11, 2015

This paper addresses local and global bifurcations that may appear in electrical power systems, such as DC microgrids, which recently has attracted interest from the electrical engineering society. Most sources in these networks are voltage-type and operate in parallel. In such configuration, the basic technique for stabilizing the bus voltage is the so-called droop control. The main contribution of this work is a codimension-two bifurcation analysis of a small DC microgrid considering the droop control gain and the power processed by the load as bifurcation parameters. The codimension-two bifurcation set leads to practical rules for achieving a robust droop control design. Moreover, the bifurcation analysis also offers a better understanding of the dynamics involved in the problem and how to avoid possible instabilities. Simulation results are presented in order to illustrate the bifurcation analysis.

Keywords: DC microgrids; droop control; constant power load; Hopf bifurcation; Takens–Bogdanov bifurcation.

1. Introduction

Microgrids are complex electrical circuits with multiple sources and loads interacting [Boroyevich *et al.*, 2013; Guerrero *et al.*, 2011]. It is a new paradigm for the electrical power system due to the presence of power converters instead of the usual synchronous machines with very large inertia. One of the advantages of microgrids, comparing with the classical electrical power system, is the presence of several sources, so the energy generation is distributed throughout the system, which makes it more reliable. The common approach to the microgrid stability analysis focuses on model linearization of each system element [Radwan & Mohamed, 2012; Lu *et al.*, 2014]. A different approach that uses large-signal stability analysis is developed in [Du *et al.*, 2013]. Other related works where bifurcation analysis techniques were applied can be found in [Xiong *et al.*, 2013a, 2013b; Gavagsaz-Ghoachani *et al.*, 2013]. In these papers, different microgrid structures and multioperating modes were considered and, despite offering a more precise model,

*Author for correspondence

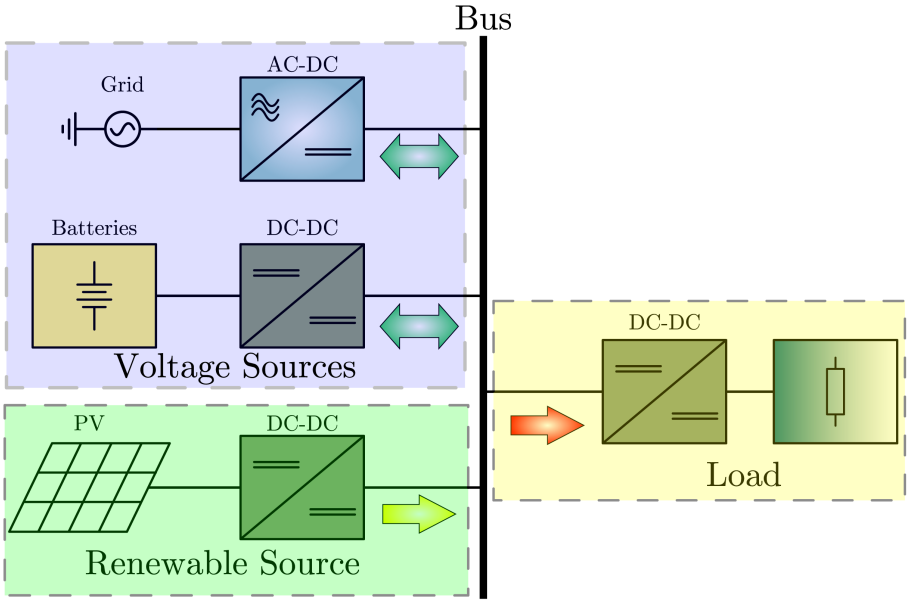

Fig. 1. The DC microgrid case study.

the number of equations becomes too large even for small microgrids and thus increases the complexity of the system analysis. This paper offers a different way to verify the system stability by neglecting the internal dynamics of each element and focusing only on the dynamics of the connection between them. Moreover, by using bifurcation analysis techniques it is possible to establish a safe power operating region and to design appropriate protection mechanisms in order to enhance the system reliability and stability.

One of the major issues in microgrids is how to share the power of two or more energy sources having a common load, also known as load sharing problem. The power that each source provides to the load is different, unless the impedance connecting the source to the load is equal. The problem of unbalanced load sharing goes from the stress of some converters to the acting of the electrical protections due to circulating currents, i.e. currents in the opposite direction of the desired power flow. For these reasons, it is interesting to equalize the power

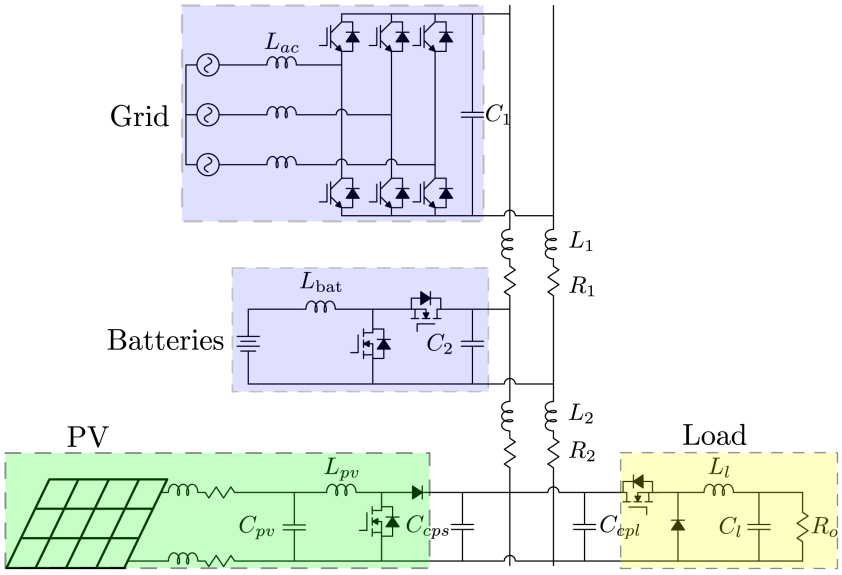

Fig. 2. DC microgrid case study showing the power converters.

driven by each source through a control technique called droop control. This control adds a virtual resistance in series with each voltage source [Dragicevic *et al.*, 2014]. If the virtual resistance prevails over any impedance connected to each source, then the power shared among the sources is approximately equal. From the control perspective, this approach increases the system damping.

The microgrid case study is a simple one: two sources, one renewable source (PhotoVoltaic system — PV) and one load (see Fig. 1). Notice that the arrows in Fig. 1 stand for the direction of the power flow for each element. Besides, Fig. 2 shows the electrical circuits of the DC microgrid from Fig. 1.

In this paper, theoretical analysis is provided for some local bifurcations along with numerical analysis regarding the study of global bifurcations. Additionally, the whole microgrid as illustrated in Fig. 2 is simulated to better understand some implications due to the modeling process. A similar problem as that presented here, but from a power electronics point of view, can be seen in [Tahim *et al.*, 2015] and for a general overview of the subject, see [Planas *et al.*, 2013].

The paper is organized as follows. In Sec. 2, the mathematical model of the microgrid case study is presented. Some local bifurcations that appear in the proposed model are analyzed in Sec. 3. Global bifurcation analysis is presented in Sec. 4. The full microgrid model is compared with the reduced model adopted in this work in Sec. 5. Section 6 is dedicated to discuss the shortcomings of the reduced model. Simulation results in order to validate the bifurcation analysis are presented in Sec. 7.

2. Equivalent Microgrid Modeling

In this microgrid case study, one of the sources is a DC-DC power converter driven by a battery pack and the other one is an AC-DC power converter connected to the main grid. Both of these sources are controlling their output voltage, so ideally they are voltage sources. The PV source behaves like a power source, injecting piecewise constant power to the microgrid, and thus it is modeled as a Constant Power Source (CPS). This source is dependent on the weather, so the power injected to the microgrid varies in steps when the weather changes.

A DC-DC power converter controlling the output voltage across a resistance is considered as the system nonlinear load. In this sense, the input terminals of this controlled power converter can be modeled as a Constant Power Load (CPL) [Onwuchekwa & Kwasinski, 2010; Zhang & Yan, 2011; Magne *et al.*, 2012]. The PV source has a similar behavior as the CPL, but injecting constant power to the microgrid instead of draining power. The CPS and CPL characteristic curves are depicted in Fig. 3. There are three operating regions for the equivalent load (CPS and CPL). The region III, which is nonlinear, is the designed operating region. The equivalent load might operate in regions I and II which are predominantly linear.

In this work, it is assumed that the static curves of the CPL and CPS have the following characteristics: (i) V_{th} has a constant value regardless of the CPL power; (ii) although V_{pv} is a function of the CPS power, it is assumed that the PV power is constant, hence V_{pv} is constant; (iii) $V_{\text{th}} > V_{\text{pv}}$.

The voltage sources internal model and their corresponding simplified models are illustrated in Figs. 4 and 5. These voltage sources are modeled by

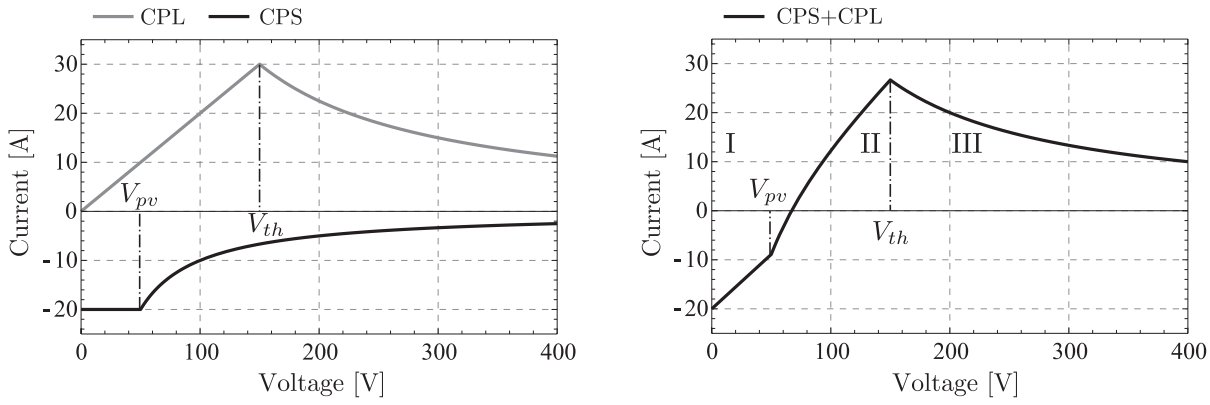

Fig. 3. CPS and CPL modeled as piecewise static characteristic curves in (V_o, I_o)-plane.

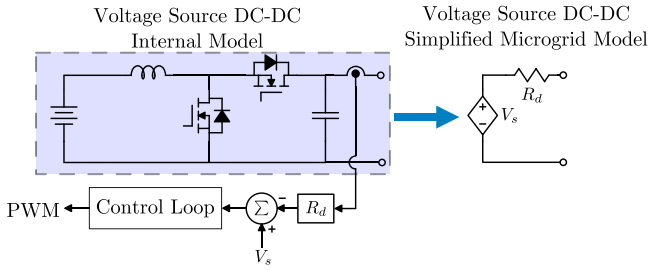

Fig. 4. The simplification modeling process of the DC-DC voltage source.

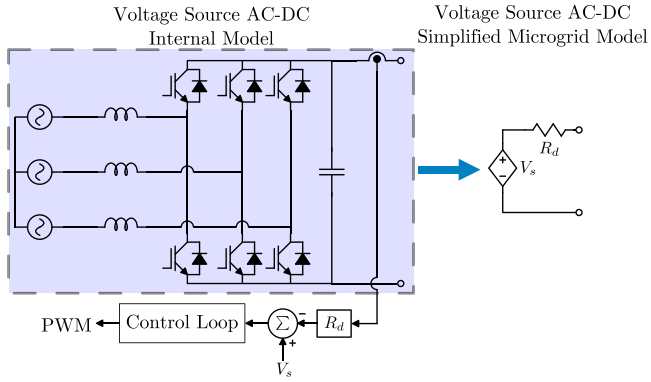

Fig. 5. The simplification modeling process of the AC-DC voltage source.

an ideal source (V_s) with a resistance in series (R_d), and this resistance is the droop control parameter. The idea behind the simplification modeling process is that there are two different time scales associated with the microgrid dynamics: (i) slow internal dynamics of the sources; (ii) fast dynamics of the transmission line and CPL loads. The DC microgrid equivalent circuit can be seen in Fig. 6. The transmission lines in the microgrid are modeled by resistive and inductive elements (R_1, R_2, L_1 and L_2), with the values of the pair $\{R_2, L_2\}$ two times greater than $\{R_1, L_1\}$. Also, the CPS and CPL have filter capacitors connected in their input terminals

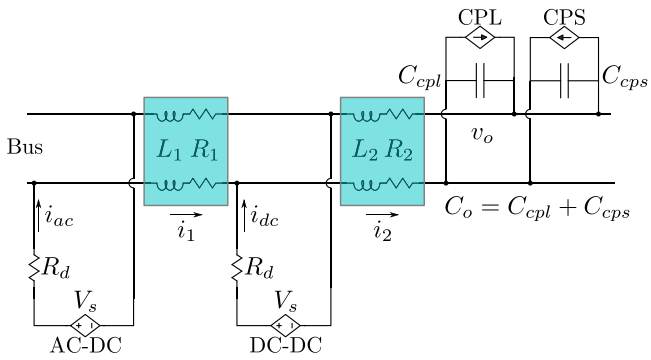

Fig. 6. The microgrid equivalent circuit.

(from the microgrid point of view) and these capacitors can be combined into a single equivalent capacitance (C_o).

The DC microgrid under consideration is described by the following equations

$$\begin{aligned} L_1\frac{di_1}{dt} &= -(R_1 + 2R_\mathrm{d})i_1 + R_\mathrm{d}i_2, \\ L_2\frac{di_2}{dt} &= R_\mathrm{d}i_1 - (R_2 + R_\mathrm{d})i_2 - v_o + V_s, \\ C_o\frac{dv_o}{dt} &= i_2 - i_o, \end{aligned} \tag{1}$$

where $i_o = i_\mathrm{cpl} + i_\mathrm{cps}$. The currents i_cpl and i_cps are defined as

$$i_\mathrm{cpl} = \begin{cases} \dfrac{P_\mathrm{cpl}}{v_o}, & \text{if } v_o \geq V_\mathrm{th} \\ \dfrac{v_o}{R_\mathrm{th}}, & \text{if } v_o < V_\mathrm{th} \end{cases} \tag{2}$$

$$i_\mathrm{cps} = \begin{cases} -\dfrac{P_\mathrm{cps}}{v_o}, & \text{if } v_o \geq V_\mathrm{pv} \\ -I_\mathrm{max}, & \text{if } v_o < V_\mathrm{pv}, \end{cases} \tag{3}$$

where P_cpl and P_cps stand for the CPL and CPS powers respectively; V_th and V_pv are the threshold voltages for the load and PV respectively, as shown in Fig. 3.

The AC-DC current source ($i_\mathrm{ac} = i_1$) and the DC-DC current source ($i_\mathrm{dc} = i_2 - i_1$) are defined in the interval $(i_\mathrm{ac}, i_\mathrm{dc}) \in (-\infty, V_s/R_\mathrm{d}]$. The bus voltage v_o is defined only for positive values ($v_o \in \mathbb{R}^+$).

The linear region of the CPL is described by $R_\mathrm{th} = V_\mathrm{th}^2/P_\mathrm{cpl}$, and the constant region of the CPS by $V_\mathrm{pv} = P_\mathrm{cps}/I_\mathrm{max}$. When both the CPL and CPS are operating in the nonlinear region, $P_o = P_\mathrm{cpl} - P_\mathrm{cps}$. Although most of the analytical bifurcation analysis focuses on the nonlinear region III, global bifurcations covering more than one operating region are analyzed by numerical methods. In this analysis, all the parameters are fixed except the droop gain, R_d, regarded as a bifurcation parameter. Furthermore, it is interesting to analyze the system to different load power values (P_o). By fixing the CPS power, the total power P_o becomes the second bifurcation parameter.

The equilibrium point (I_1, I_2, V_o) of (1) is defined by

$$I_1 = \frac{R_\mathrm{d}}{R_1 + 2R_\mathrm{d}}\frac{V_s - V_o}{R_\mathrm{eq}}, \quad I_2 = \frac{V_s - V_o}{R_\mathrm{eq}},$$

with

$$R_{\text{eq}} = \frac{R_1R_2 + R_1R_{\text{d}} + 2R_2R_{\text{d}} + R_{\text{d}}^2}{R_1 + 2R_{\text{d}}}. \tag{4}$$

Note that V_o varies according to the region of operation. In region III, this voltage is given by

$$V_o^2 - V_sV_o + R_{\text{eq}}P_o = 0, \tag{5}$$

therefore, there are two equilibrium points, (I_1, I_2, V_o^+) and (I_1, I_2, V_o^-), where $V_o^\pm$ is given by

$$V_o^\pm = \frac{V_s}{2} \pm \sqrt{\frac{V_s^2}{4} - R_{\text{eq}}P_o}, \tag{6}$$

provided that $V_s^2/4 \geq R_{\text{eq}}P_o$, i.e. the maximum power the system can handle is dictated by

$$P_{\max} = \frac{V_s^2}{4R_{\text{eq}}}. \tag{7}$$

In region II, system (1) has only one equilibrium point with

$$V_o = \frac{V_s}{2}\frac{R_{\text{th}}}{R_{\text{th}} + R_{\text{eq}}} + \sqrt{\frac{R_{\text{th}}}{R_{\text{th}} + R_{\text{eq}}}\left(\frac{V_s^2}{4}\frac{R_{\text{th}}}{R_{\text{th}} + R_{\text{eq}}} + R_{\text{eq}}P_{\text{cps}}\right)}, \tag{8}$$

since the other root is outside the domain of v_o ($v_o \in \mathbb{R}^+$). In region I, the system also has only one equilibrium point with

$$V_o = \frac{R_{\text{th}}R_{\text{eq}}}{R_{\text{th}} + R_{\text{eq}}}\left(I_{\max} + \frac{V_s}{R_{\text{eq}}}\right). \tag{9}$$

The number of equilibria changes when the load goes from one region to another, and it is expected that some global bifurcations appear. A diagram of the evolution of the equilibrium points V_o^+ and V_o^- as the parameter P_{cpl} varies is shown in Fig. 7(a). This picture illustrates the changes on system's equilibria that the transition from regions II to III causes in the system model. The area between the vertical dashed-dot lines [Fig. 7(a)] is the only area where there exist three equilibrium points. Another way to see the relationship between the number of equilibrium points and CPL power is to plot a set of static curves for different P_{cpl} values together with the equilibrium equation, as can be seen in Fig. 7(b). It shows that for $P_{\text{cpl}} = 33\,\text{kW}$ there are three equilibrium points, but for other values of power ($P_{\text{cpl}} = 10\,\text{kW}$ and $P_{\text{cpl}} = 55\,\text{kW}$) there is only one.

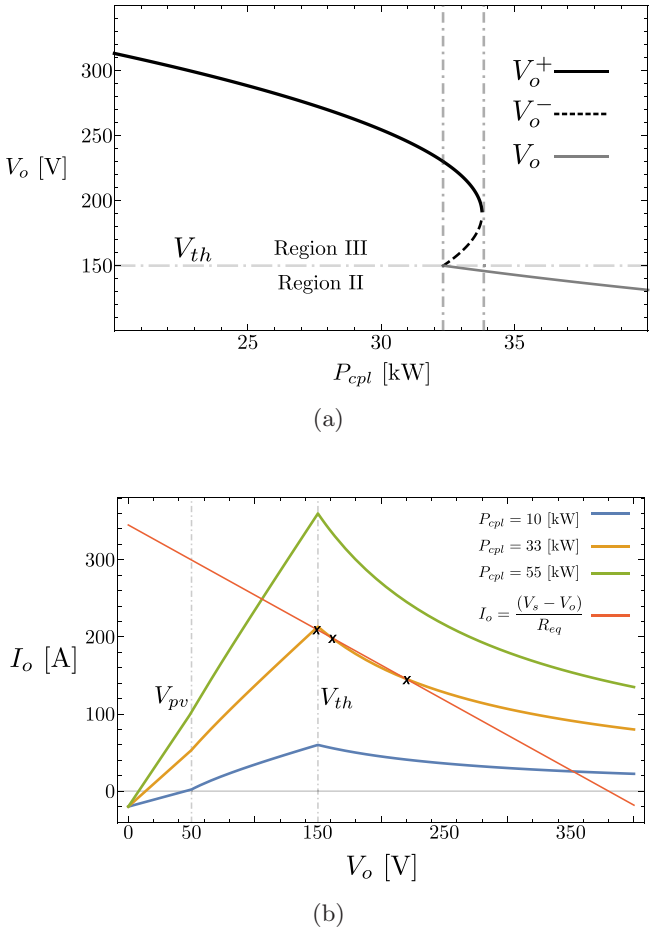

Fig. 7. Equilibrium points of system (1) in (a) (P_{cpl}, V_o)-plane and (b) (V_o, I_o)-plane.

3. Local Bifurcation Analysis

In this section, standard local bifurcation analysis is developed for system (1). This system is normalized so that any change of variables can be defined disregarding the physical dimension of the process. The relation between the normalized and original variables are

$$\iota_1 = \frac{\omega_b L_2}{V_s} i_1, \quad \iota_2 = \frac{\omega_b L_2}{V_s} i_2, \quad \nu_o = \frac{v_o}{V_s},$$

with time $t = \tau\sqrt{L_2C_o}$. Defining the new parameters

$$\omega_b = \frac{1}{\sqrt{L_2C_o}}, \quad r_1 = \frac{R_1}{\omega_b L_2}, \quad r_2 = \frac{R_2}{\omega_b L_2},$$

$$p_o = P_o\frac{\omega_b L_2}{V_s^2}, \quad p_{\text{cps}} = P_{\text{cps}}\frac{\omega_b L_2}{V_s^2},$$

the normalized model is given by

$$\frac{d\iota_1}{d\tau} = -2\left(\frac{r_2}{2} + 2r_{\text{d}}\right)\iota_1 + 2r_{\text{d}}\iota_2,$$

$$\frac{d\iota_2}{d\tau} = r_{\rm d}\iota_1 - (r_2 + r_{\rm d})\iota_2 - \nu_o + 1,$$
$$\frac{d\nu_o}{d\tau} = \iota_2 - \iota_o, \tag{10}$$

with

$$\iota_o = \begin{cases} \dfrac{p_o}{\nu_o}, & \text{if } \nu_o \geq \mathcal{V}_{\rm th} \\ \dfrac{\nu_o}{r_{\rm th}} - \dfrac{p_{\rm cps}}{\nu_o}, & \text{if } \mathcal{V}_{\rm pv} \leq \nu_o < \mathcal{V}_{\rm th} \\ \dfrac{\nu_o}{r_{\rm th}} - \iota_{\max}, & \text{if } \nu_o < \mathcal{V}_{\rm pv}, \end{cases} \tag{11}$$

where $\mathcal{V}_{\rm th} = V_{\rm th}/V_s$ and $\mathcal{V}_{\rm pv} = V_{\rm pv}/V_s$. The normalized equilibria are given by $(\mathcal{I}_1, \mathcal{I}_2, \mathcal{V}_o)$. Note that, the normalized equilibria are assigned by calligraphy symbols and the denormalized equilibria by roman symbols.

A new change of variables is applied to (10) in order to translate the equilibrium points of this system to the origin as follows

$$y_1 = \iota_1 - \mathcal{I}_1, \quad y_2 = \iota_2 - \mathcal{I}_2, \quad y_3 = \nu_o - \mathcal{V}_o$$

and by separating the linear part from the nonlinear one, the differential equations become

$$\frac{dy_1}{d\tau} = -(r_2 + 4r_{\rm d})y_1 + 2r_{\rm d}y_2,$$
$$\frac{dy_2}{d\tau} = r_{\rm d}y_1 - (r_2 + r_{\rm d})y_2 - y_3, \tag{12}$$
$$\frac{dy_3}{d\tau} = y_2 + g_o y_3 - g_o \frac{y_3^2}{y_3 + \mathcal{V}_o},$$

with $g_o = p_o/\mathcal{V}_o^2$.

In matricial form, the model is given by $\dot{y}_i = A_{ij}y_j + F_i(y_3)$, with $i, j \in \{1, 2, 3\}$ representing the components of a vector or matrix, and $\dot{y}$ is the derivative with respect to normalized time. Repeated indices indicate summation. The linear part of (12) is

$$A_{ij} = \begin{pmatrix} -(r_2 + 4r_{\rm d}) & 2r_{\rm d} & 0 \\ r_{\rm d} & -(r_2 + r_{\rm d}) & -1 \\ 0 & 1 & g_o \end{pmatrix},$$

whereas the nonlinear part is

$$F_i(y_3) = \frac{y_3^2}{\mathcal{V}_o + y_3} \begin{pmatrix} 0 \\ 0 \\ -g_o \end{pmatrix}.$$

Local bifurcations found for this microgrid model can be classified by analyzing the coefficients of the characteristic polynomial:

$$\Delta(\lambda) = \lambda^3 + a_2\lambda^2 + a_1\lambda + a_0, \tag{13}$$

with

$$a_2 = 2r_2 + 5r_{\rm d} - g_o,$$
$$a_1 = 1 + r_{\rm eq}(r_2 + 4r_{\rm d}) - g_o(2r_2 + 5r_{\rm d}),$$
$$a_0 = (r_2 + 4r_{\rm d})(1 - g_o r_{\rm eq})$$

and $r_{\rm eq} = (r_2^2 + 5r_2r_{\rm d} + 2r_{\rm d}^2)/(r_2 + 4r_{\rm d})$.

There are three local bifurcations that can be found by analyzing the equilibria of (5) and the coefficients of (13): (i) saddle-node of equilibrium points (SN), (ii) Hopf bifurcation (HB) and (iii) Takens–Bogdanov (TB). Based on these coefficients it is possible to find the system of normal form for each bifurcation.

The set of codimension-two local bifurcations in $(P_o, R_{\rm d})$-plane with P_o and $R_{\rm d}$, with the original bifurcation parameters of system (1), is depicted in Fig. 8.

The Hopf bifurcation for the normalized system is found by solving $a_1a_2 = a_0$ for $r_{\rm d}$ and p_o, and for the saddle-node, (7) is used to generate the curve, valid for the original system.

3.1. *Saddle-node bifurcation*

There are two equilibrium points $(\mathcal{V}_o^+, \mathcal{V}_o^-)$ in the nonlinear region whenever $p_o \leq p_{\max}$, one stable branch and the other is unstable. Both branches join at the maximum power point where the saddle-node bifurcation occurs ($a_0 = 0$ when $p_o = p_{\max}$). The equilibrium $\mathcal{V}_o^-$ corresponds to the unstable

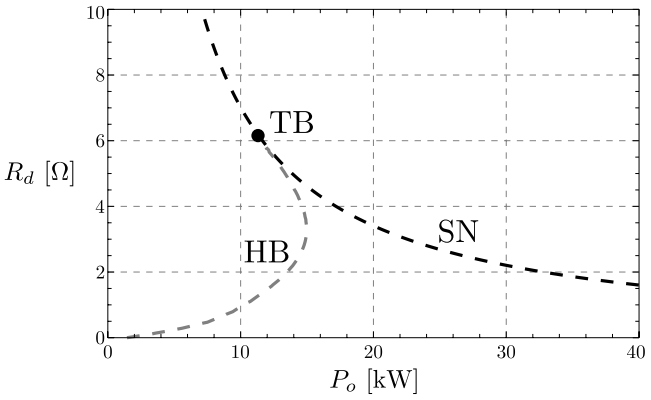

Fig. 8. Codimension-two bifurcation set for P_o and $R_{\rm d}$ as bifurcation parameters assuming that the other system parameters are given in Table 1 of Sec. 7.

equilibrium branch since $a_0 < 0$, and $\mathcal{V}_o^+$ is the stable branch because $a_0 > 0$. As the load static curve is piecewise (see Fig. 3), the unstable branch does not exist for all values of p_o, i.e. whenever the voltage $\mathcal{V}_o$ becomes too small, the load characteristic changes at $\nu_o = \mathcal{V}_{\text{th}}$ and $\nu_o = \mathcal{V}_{\text{pv}}$, or $v_o = V_{\text{th}}$ and $v_o = V_{\text{pv}}$ for the original equations as shown in (2) and (3).

The normal form for the saddle-node bifurcation can be obtained by nonlinear transformations valid locally at the bifurcation point. The numerical values for the parameters r_{d} and p_o can be selected using Fig. 8. So at saddle-node bifurcation point, the characteristic polynomial is

$$\begin{aligned}\Delta_{\text{sn}}(\lambda) &= \lambda(\lambda^2 + a_2\lambda + a_1)\\ &= \lambda(\lambda+\sigma)(\lambda+\zeta).\end{aligned}$$

The parameters σ and ζ are

$$\begin{aligned}\sigma = \frac{1}{2}\Big\{&2r_2 + 5r_{\text{d}} - g_o\\ &+ \sqrt{g_o^2 + 4g_o r_2 + 10 g_o r_{\text{d}} + 17 r_{\text{d}}^2 - 4}\Big\},\\ \zeta = \frac{1}{2}\Big\{&2r_2 + 5r_{\text{d}} - g_o\\ &- \sqrt{g_o^2 + 4g_o r_2 + 10 g_o r_{\text{d}} + 17 r_{\text{d}}^2 - 4}\Big\},\end{aligned}$$

where σ and ζ are real and positive (for instance, selecting a large value for r_{d}), thus Hopf bifurcation does not occur. System (12) can be expressed in the Jordan canonical form through the transformation $y_i = T_{ij}x_j$:

$$\begin{aligned}\dot{y}_i &= A_{ij}y_j + F_i(y_3)\\ \dot{x}_i &= T_{ij}^{-1}A_{jk}T_{kl}x_l + T_{ij}^{-1}F_j(T_{3j}x_j)\\ \dot{x}_i &= J_{ij}x_j + s_i f(x),\end{aligned}$$

where

$$J_{ij} = \begin{pmatrix}-\sigma & 0 & 0\\ 0 & -\zeta & 0\\ 0 & 0 & 0\end{pmatrix}, \quad s_i = \begin{pmatrix}s_1\\ s_2\\ s_3\end{pmatrix}$$

and $f(x)$ is given by

$$f(x) = \frac{(x_1 + x_2 + x_3)^2}{\mathcal{V}_o + x_1 + x_2 + x_3}.$$

The transformation T_{ij} is

$$T_{ij} = \begin{pmatrix}-\dfrac{2r_{\text{d}}(\sigma+g_o)}{r_2 + r_{\text{d}} - \sigma} & -\dfrac{2r_{\text{d}}(\zeta+g_o)}{r_2 + r_{\text{d}} - \zeta} & -\dfrac{2r_{\text{d}}g_o}{r_2 + r_{\text{d}}}\\ -\sigma - g_o & -\zeta - g_o & -g_o\\ 1 & 1 & 1\end{pmatrix}.$$

In this analysis only the parameter s_3, given by

$$s_3 = -\frac{(r_2 + 4r_{\text{d}})(g_o + r_2 + 4r_{\text{d}})}{-g_o^2(2r_2 + 5r_{\text{d}}) + g_o(-3r_2 r_{\text{d}} - 16r_{\text{d}}^2 + 1) + r_2^3 + 9r_2^2 r_{\text{d}} + 22 r_2 r_{\text{d}}^2 + 8r_{\text{d}}^3},$$

is necessary. Notice that F_i is a vector function, whereas $f(x)$ is just a scalar function ($T_{ij}^{-1}F_j = s_i f$).

Expanding $f(x)$ into a Taylor series and applying the center manifold theorem [Guckenheimer & Holmes, 1983], which is used to reduce the order of (12), it is possible to reach the following result, by neglecting high order terms,

$$f(x) = \frac{1}{\mathcal{V}_o}x_3^2 + \mathcal{O}(3).$$

The normal form of the microgrid model at the saddle-node bifurcation point is

$$\dot{x}_3 = \frac{s_3}{\mathcal{V}_o}x_3^2 + \mathcal{O}(3). \tag{14}$$

The parameter s_3 is negative implying that for positive initial conditions, x_3 converges to the origin, and for negative initial conditions, the system diverges.

3.2. *Hopf bifurcation*

In order to analyze the Hopf bifurcation, the theory of normal forms is used to identify the type of limit cycle (unstable or stable) that appears in system (12), when the condition $a_1 a_2 = a_0$, with $a_0 > 0$ and $a_2 > 0$ is satisfied.

The characteristic polynomial at the Hopf bifurcation point is

$$\begin{aligned}\Delta_h(\lambda) &= (\lambda+\sigma)(\lambda^2 + \omega_h^2),\\ \sigma &= 2r_2 + 5r_{\text{d}} - g_o,\\ \omega_h^2 &= 1 + r_2^2 + 5r_2 r_{\text{d}} + 2r_{\text{d}}^2 - g_o(2r_2 + 5r_{\text{d}}).\end{aligned}$$

Notice that, the parameter σ used before for the saddle-node normal form is utilized again for the Hopf normal form. Consequently, in this section this parameter has a different value. The same

consideration is used for the Takens–Bogdanov normal form. This parameter always represents a stable eigenvalue regardless of its value.

System (12) can be transformed in the Jordan canonical form by

$$T_{ij} = \begin{pmatrix} \dfrac{2r_{\rm d}(2r_2+5r_{\rm d})}{r_2+r_{\rm d}-g_o} & \dfrac{2r_{\rm d}\{(r_2+4r_{\rm d})(\omega_h-g_o)+\omega_h(\omega_h+g_o)\}}{(r_2+4r_{\rm d})^2+\omega_h^2} & \dfrac{-2r_{\rm d}\{(r_2+4r_{\rm d})(\omega_h+g_o)-\omega_h(\omega_h-g_o)\}}{(r_2+4r_{\rm d})^2+\omega_h^2} \\ -5r_{\rm d}-2r_2 & -g_o+\omega_h & -g_o-\omega_h \\ 1 & 1 & 1 \end{pmatrix},$$

which results in $\dot{x}_i = J_{ij}x_j + \kappa_i f(x)$, where

$$J_{ij} = \begin{pmatrix} -\sigma & 0 & 0 \\ 0 & 0 & -\omega_h \\ 0 & \omega_h & 0 \end{pmatrix}, \quad \kappa_i = \begin{pmatrix} \kappa_1 \\ \kappa_2 \\ \kappa_3 \end{pmatrix}$$

and

$$f(x) = \frac{(x_1+x_2+x_3)^2}{\mathcal{V}_o+x_1+x_2+x_3},$$

$$\kappa_1 = -\frac{g_o(g_o^2+\omega_h^2)(g_o-r_2-r_{\rm d})}{(g_o+r_2+4r_{\rm d})\{g_o^2-2g_o[2r_2+5r_{\rm d}]+4r_2^2+20r_2r_{\rm d}+25r_{\rm d}^2+\omega_h^2\}},$$

$$\begin{aligned}\kappa_2 = {} & \frac{g_o(2r_2+5r_{\rm d})}{2\omega_h(g_o+r_2+4r_{\rm d})\{g_o^2-2g_o[2r_2+5r_{\rm d}]+4r_2^2+20r_2r_{\rm d}+25r_{\rm d}^2+\omega_h^2\}} \\ & \times\{g_o^2(r_2+4r_{\rm d}+\omega_h)-g_o(2r_2^2+13r_2r_{\rm d}+20r_{\rm d}^2-3r_{\rm d}\omega_h+2\omega_h^2) \\ & -\omega_h(2r_2^2+13r_2r_{\rm d}-r_2\omega_h+20r_{\rm d}^2-r_{\rm d}\omega_h+\omega_h^2)\},\end{aligned}$$

$$\begin{aligned}\kappa_3 = {} & -\frac{g_o(2r_2+5r_{\rm d})}{2\omega_h(g_o+r_2+4r_{\rm d})\{g_o^2-2g_o[2r_2+5r_{\rm d}]+4r_2^2+20r_2r_{\rm d}+25r_{\rm d}^2+\omega_h^2\}} \\ & \times\{g_o^2(r_2+4r_{\rm d}-\omega_h)-g_o(2r_2^2+13r_2r_{\rm d}+20r_{\rm d}^2+3r_{\rm d}\omega_h+2\omega_h^2) \\ & +\omega_h(2r_2^2+13r_2r_{\rm d}+r_2\omega_h+20r_{\rm d}^2+r_{\rm d}\omega_h+\omega_h^2)\}.\end{aligned}$$

The nonlinear part, $f(x)$, can be expanded into a Taylor series up to the cubic terms, because high order terms are not necessary for the Hopf bifurcation analysis. Thus, only the following terms of $f(x)$ are considered

$$f(x) = \frac{1}{\mathcal{V}_o}\{x_2^2+x_3^2+2x_2x_3+2x_1(x_2+x_3)\} + \frac{1}{\mathcal{V}_o^2}\{x_2^3+x_3^3+3x_2^2x_3+3x_2x_3^2\} + \mathcal{O}(4).$$

Applying the center manifold theorem, $x_1 = h(x_2, x_3)$, the quasilinear partial differential equation for the map h is given by

$$\mathcal{N}(x) = \frac{\partial h}{\partial x_2}[-\omega_h x_3 + \kappa_2 f(x)] + \frac{\partial h}{\partial x_3}[\omega_h x_2 + \kappa_3 f(x)] + \sigma h - \kappa_1 f(x) = 0. \tag{15}$$

The map h can be approximated to

$$h = \alpha_{20}x_2^2 + \alpha_{11}x_2x_3 + \alpha_{02}x_3^2 + \mathcal{O}(3).$$

To find the coefficients α_{ij} is necessary to solve $\mathcal{N}(x)$ until the second order terms. The parameters α_{ij} can be found through

$$\omega_h\left(x_2\frac{\partial h}{\partial x_3} - x_3\frac{\partial h}{\partial x_2}\right) + \sigma h - \kappa_1 f_2(x_i) = 0, \quad (16)$$

where $f_2(x)$ represents the quadratic terms of $f(x)$:

$$f(x) = f_2(x) + f_3(x) + \mathcal{O}(4)$$

$$f_2(x) = \frac{x_2^2 + x_3^2 + 2x_2x_3}{\mathcal{V}_o}$$

and the cubic term is

$$f_3(x) = -\frac{x_2^3 + x_3^3 + 3x_2^2x_3 + 3x_2x_3^2}{\mathcal{V}_o^2} + \frac{2(x_2 + x_3)}{\mathcal{V}_o}h.$$

The coefficients α_{ij} are given by

$$\alpha_{20} = \frac{\kappa_1(\sigma^2 - 2\sigma\omega_h + 4\omega_h^2)}{\sigma\mathcal{V}_o(4\omega_h^2 + \sigma^2)},$$

$$\alpha_{11} = \frac{2\kappa_1\sigma}{\mathcal{V}_o(4\omega_h^2 + \sigma^2)},$$

$$\alpha_{02} = \frac{\kappa_1(\sigma^2 + 2\sigma\omega_h + 4\omega_h^2)}{\sigma\mathcal{V}_o(4\omega_h^2 + \sigma^2)}.$$

In the center manifold, $\dot{x}_2$ and $\dot{x}_3$ are

$$\begin{aligned}\dot{x}_2 = {} & -\omega_h x_3 + \frac{\kappa_2}{\mathcal{V}_o}\{x_2^2 + x_3^2 + 2x_2x_3\} \\ & + \frac{\kappa_2}{\mathcal{V}_o^2}\left\{\left[-1 + \frac{2\kappa_1(\sigma^2 - 2\sigma\omega_h + 4\omega_h^2)}{(4\omega_h^2 + \sigma^2)\sigma}\right]x_2^3\right. \\ & + \left[-3 + \frac{2\kappa_1(3\sigma^2 - 2\sigma\omega_h + 4\omega_h^2)}{(4\omega_h^2 + \sigma^2)\sigma}\right]x_2^2x_3 \\ & + \left[-3 + \frac{2\kappa_1(3\sigma^2 + 2\sigma\omega_h + 4\omega_h^2)}{(4\omega_h^2 + \sigma^2)\sigma}\right]x_2x_3^2 \\ & \left. + \left[-1 + \frac{2\kappa_1(\sigma^2 + 2\sigma\omega_h + 4\omega_h^2)}{(4\omega_h^2 + \sigma^2)\sigma}\right]x_3^3\right\} \\ & + \mathcal{O}(4), \end{aligned} \quad (17)$$

$$\begin{aligned}\dot{x}_3 = {} & \omega_h x_2 + \frac{\kappa_3}{\mathcal{V}_o}\{x_2^2 + x_3^2 + 2x_2x_3\} \\ & + \frac{\kappa_3}{\mathcal{V}_o^2}\left\{\left[-1 + \frac{2\kappa_1(\sigma^2 - 2\sigma\omega_h + 4\omega_h^2)}{(4\omega_h^2 + \sigma^2)\sigma}\right]x_2^3\right. \\ & + \left[-3 + \frac{2\kappa_1(3\sigma^2 - 2\sigma\omega_h + 4\omega_h^2)}{(4\omega_h^2 + \sigma^2)\sigma}\right]x_2^2x_3 \\ & + \left[-3 + \frac{2\kappa_1(3\sigma^2 + 2\sigma\omega_h + 4\omega_h^2)}{(4\omega_h^2 + \sigma^2)\sigma}\right]x_2x_3^2 \\ & \left. + \left[-1 + \frac{2\kappa_1(\sigma^2 + 2\sigma\omega_h + 4\omega_h^2)}{(4\omega_h^2 + \sigma^2)\sigma}\right]x_3^3\right\} \\ & + \mathcal{O}(4). \end{aligned} \quad (18)$$

To apply the normal form for the Hopf bifurcation, these equations can be described in complex form, $z = x_2 + jx_3$, with $\overline{z} = x_2 - jx_3$ being the complex conjugate of z ($j = \sqrt{-1}$). Equations (17) and (18) become

$$\dot{z} = j\omega_h z + f_2 + f_3 + \mathcal{O}(4),$$

$$f_2 = a_{20}z^2 + a_{11}z\overline{z} + a_{02}\overline{z}^2,$$

$$f_3 = b_{30}z^3 + b_{21}z^2\overline{z} + b_{12}z\overline{z}^2 + b_{03}\overline{z}^3.$$

a_{ij} and b_{ij} are complex parameters given by

$$a_{20} = \frac{\kappa_3 - j\kappa_2}{2\mathcal{V}_o}, \quad (19)$$

$$a_{11} = \frac{\kappa_2 + j\kappa_3}{\mathcal{V}_o}, \quad (20)$$

$$a_{02} = \frac{-\kappa_3 + j\kappa_2}{2\mathcal{V}_o} \quad (21)$$

and

$$b_{30} = -\frac{(1+j)(\kappa_2 + j\kappa_3)(2\kappa_1 - \sigma - j2\omega_h)}{4\mathcal{V}_o^2(\sigma + j2\omega_h)}, \quad (22)$$

$$b_{21} = \frac{(1+j)(\kappa_2 + j\kappa_3)(-j6\kappa_1\sigma + 8\kappa_1\omega_h + j3\sigma^2 - 6\sigma\omega_h)}{4\sigma\mathcal{V}_o^2(\sigma + j2\omega_h)}, \quad (23)$$

$$b_{12} = \frac{(1+j)(\kappa_2 + j\kappa_3)(6\kappa_1\sigma - j8\kappa_1\omega_h - 3\sigma^2 + j6\sigma\omega_h)}{4\sigma\mathcal{V}_o^2(\sigma - j2\omega_h)}, \quad (24)$$

$$b_{03} = \frac{(1+j)(\kappa_3 - j\kappa_2)(-2\kappa_1 + \sigma - j2\omega_h)}{4\mathcal{V}_o^2(\sigma - j2\omega_h)}. \quad (25)$$

The Hopf normal form can be found by transforming z to

$$z = w + h_2(w, \overline{w}), \tag{26}$$

so the dynamics of w is

$$\dot{z} = \dot{w} + \frac{\partial h_2}{\partial w}\dot{w} + \frac{\partial h_2}{\partial \overline{w}}\dot{\overline{w}}$$

$$\dot{z} = \left(1 + \frac{\partial h_2}{\partial w}\right)\dot{w} + \frac{\partial h_2}{\partial \overline{w}}\dot{\overline{w}}$$

$$\dot{w} = \left(1 + \frac{\partial h_2}{\partial w}\right)^{-1}\left(\dot{z} - \frac{\partial h_2}{\partial \overline{w}}\dot{\overline{w}}\right).$$

Substituting $\dot{z}$, $\dot{w}$ becomes

$$\dot{w} = \left[1 + \frac{\partial h_2}{\partial w}\right]^{-1} \times \left[j\omega_h(w + h_2) + f_2 + f_3 - \frac{\partial h_2}{\partial \overline{w}}\dot{\overline{w}}\right] + \mathcal{O}(4). \tag{27}$$

The map h_2 is quadratic, $h_2 = c_{20}w^2 + c_{02}\overline{w}^2 + c_{11}w\overline{w}$, so replacing (26) in f_2 and f_3 gives

$$f_2 = a_{20}w^2 + a_{11}w\overline{w} + a_{02}\overline{w}^2 + (2a_{20}wh_2 + a_{11}w\overline{h}_2 + a_{11}\overline{w}h_2 + 2a_{02}\overline{w}\overline{h}_2),$$

$$f_3 = b_{30}w^3 + b_{21}w^2\overline{w} + b_{12}w\overline{w}^2 + b_{03}\overline{w}^3.$$

It is necessary to rearrange these polynomials properly, considering now that the last part of f_2 is of cubic order. Thus,

$$g_2 = a_{20}w^2 + a_{11}w\overline{w} + a_{02}\overline{w}^2$$

$$g_3 = b_{30}w^3 + b_{21}w^2\overline{w} + b_{12}w\overline{w}^2 + b_{03}\overline{w}^3 + 2a_{20}wh_2 + a_{11}w\overline{h}_2 + a_{11}\overline{w}h_2 + 2a_{02}\overline{w}\overline{h}_2,$$

wherein g_2 is a second order polynomial and g_3 a third order one ($f_2 + f_3 = g_2 + g_3$).

Using the definition of h_2, g_3 becomes

$$g_3 = (b_{30} + 2a_{20}c_{20} + a_{11}\bar{c}_{02})w^3 + (b_{21} + 2a_{20}c_{11} + a_{11}\bar{c}_{11} + a_{11}c_{20} + 2a_{02}\bar{c}_{02})w^2\overline{w} + (b_{12} + 2a_{20}c_{02} + a_{11}\bar{c}_{20} + a_{11}c_{11} + 2a_{02}\bar{c}_{11})w\overline{w}^2 + (b_{03} + a_{11}c_{02} + 2a_{02}\bar{c}_{20})\overline{w}^3,$$

that can be written as $g_3 = d_{30}w^3 + d_{21}w^2\overline{w} + d_{12}w\overline{w}^2 + d_{03}\overline{w}^3$.

The term $[1 + \partial h_2/\partial w]^{-1}$ of (27) can be expanded into a Taylor series:

$$\left[1 + \frac{\partial h_2}{\partial w}\right]^{-1} = 1 - (2c_{20}w + c_{11}\overline{w}) + (4c_{20}^2w^2 + c_{11}^2\overline{w}^2 + 4c_{20}c_{11}w\overline{w}) + \mathcal{O}(3) = 1 - \frac{\partial h_2}{\partial w} + m_2 + \mathcal{O}(3),$$

where $\partial h_2/\partial w$ is first order and m_2 is quadratic.

The dynamics of $\overline{w}$ is not known, but it has the following form:

$$\dot{\overline{w}} = \overline{\lambda}\overline{w} + \overline{n}_2 + \overline{n}_3 + \mathcal{O}(4),$$

where $\lambda = j\omega_h$. The mappings n_2 and n_3 are still unknown and they correspond to the second and third order nonlinear parts, respectively.

Based on (27), the required part of $\dot{\overline{w}}$ is

$$\left[1 + \frac{\partial h_2}{\partial w}\right]^{-1}\frac{\partial h_2}{\partial \overline{w}}\dot{\overline{w}} = \left\{\overline{\lambda}\frac{\partial h_2}{\partial \overline{w}}\overline{w}\right\} + \left\{\frac{\partial h_2}{\partial \overline{w}}\overline{n}_2 - \overline{\lambda}\frac{\partial h_2}{\partial w}\frac{\partial h_2}{\partial \overline{w}}\overline{w}\right\} + \mathcal{O}(4).$$

To cancel all the second order terms, n_2 must be null, therefore

$$\dot{w} = \lambda w + \left\{\lambda h_2 - \lambda\frac{\partial h_2}{\partial w}w - \overline{\lambda}\frac{\partial h_2}{\partial \overline{w}}\overline{w} + g_2\right\} + \left\{\lambda m_2 w - \lambda\frac{\partial h_2}{\partial w}h_2 - \frac{\partial h_2}{\partial w}g_2 + \overline{\lambda}\frac{\partial h_2}{\partial w}\frac{\partial h_2}{\partial \overline{w}}\overline{w} + g_3\right\} + \mathcal{O}(4).$$

It follows that the second order terms can be annihilated by choosing the coefficients of h_2 according to

$$c_{20} = \frac{a_{20}}{\lambda}, \quad c_{02} = -\frac{a_{02}}{3\lambda}, \quad c_{11} = -\frac{a_{11}}{\lambda},$$

where the parameters a_{ij} are given by (19)–(21). This is the solution of the homological equation:

$$\lambda h_2 - \lambda\frac{\partial h_2}{\partial w}w - \overline{\lambda}\frac{\partial h_2}{\partial \overline{w}}\overline{w} + g_2 = 0.$$

The remaining cubic terms are given by

$$\left\{\lambda m_2 w - \lambda\frac{\partial h_2}{\partial w}h_2 - \frac{\partial h_2}{\partial w}g_2 + \overline{\lambda}\frac{\partial h_2}{\partial w}\frac{\partial h_2}{\partial \overline{w}}\overline{w} + g_3\right\} = g_3,$$

thus the nonlinear part has been simplified up to the third order terms:

$$\dot{w} = \lambda w + d_{30}w^3 + d_{21}w^2\overline{w} + d_{12}w\overline{w}^2 + d_{03}\overline{w}^3 + \mathcal{O}(4). \tag{28}$$

The third order terms can be annihilated, with the exception of $w^2\overline{w}$ [Kuznetsov, 2004], by the following change of variables:

$$w = \xi + h_3,$$
$$h_3 = q_{30}\xi^3 + q_{03}\overline{\xi}^3 + q_{12}\xi\overline{\xi}^2.$$

The dynamics of ξ is

$$\dot{\xi} = \lambda\xi + d_{21}\xi^2\overline{\xi} + \left\{\lambda h_3 - \lambda\frac{\partial h_3}{\partial\xi}\xi - \overline{\lambda}\frac{\partial h_3}{\partial\overline{\xi}}\overline{\xi} + d_{30}\xi^3 + d_{12}\xi\overline{\xi}^2 + d_{03}\overline{\xi}^3\right\} + \mathcal{O}(4). \tag{29}$$

Choosing the coefficients q_{ij} as

$$q_{30} = \frac{d_{30}}{2\lambda},$$
$$q_{03} = -\frac{d_{03}}{4\lambda},$$
$$q_{12} = -\frac{d_{12}}{2\lambda},$$

then

$$\dot{\xi} = \lambda\xi + d_{21}\xi^2\overline{\xi} + \mathcal{O}(4). \tag{30}$$

Transforming (30) into cylindrical coordinates, $\xi = \rho\exp(j\theta)$ with $d_{21}^R = \mathrm{Re}\{d_{21}\}$ and $d_{21}^I = \mathrm{Im}\{d_{21}\}$, it becomes

$$\dot{\rho} = d_{21}^R\rho^3 + \mathcal{O}(5),$$
$$\dot{\theta} = \omega_h + d_{21}^I\rho^2 + \mathcal{O}(4),$$

where

$$d_{21}^R = \frac{1}{4\sigma\omega_h\mathcal{V}_o^2(\sigma^2+4\omega_h^2)}\{\kappa_2\omega_h[2\kappa_1(3\sigma^2 - 2\sigma\omega_h + 8\omega_h^2) - 3(\sigma^3 + 4\sigma\omega_h^2)] + \kappa_3\{\omega_h[2\kappa_1(3\sigma^2 + 2\sigma\omega_h + 8\omega_h^2) - 3(\sigma^3 + 4\sigma\omega_h^2)] - 2\kappa_3(\sigma^3 + 4\sigma\omega_h^2)\} + 2\kappa_2^2(\sigma^3 + 4\sigma\omega_h^2)\}, \tag{31}$$

$$d_{21}^I = -\frac{1}{12\sigma\omega_h\mathcal{V}_o^2(\sigma^2+4\omega_h^2)}\{\kappa_3[3\omega_h(-6\kappa_1\sigma^2 + 4\kappa_1\sigma\omega_h - 16\kappa_1\omega_h^2 + 3\sigma^3 + 12\sigma\omega_h^2) + 14\kappa_3(\sigma^3 + 4\sigma\omega_h^2)] - 3\kappa_2\{\omega_h[3(\sigma^3 + 4\sigma\omega_h^2) - 2\kappa_1(3\sigma^2 + 2\sigma\omega_h + 8\omega_h^2)] + 4\kappa_3(\sigma^3 + 4\sigma\omega_h^2)\} + 14\kappa_2^2(\sigma^3 + 4\sigma\omega_h^2)\}. \tag{32}$$

The stability of the periodic orbit is given by the real part of d_{21} which, in this case, is positive, indicating a subcritical Hopf bifurcation. However, there is a global bifurcation that limits the amplitude of this unstable periodic orbit arising from the Hopf bifurcation, for a given value of the parameter p_o, as will be seen in Sec. 4.

3.3. *Takens–Bogdanov bifurcation*

The characteristic polynomial of the linear part of the system at the point where the Takens–Bogdanov bifurcation occurs is given by

$$\Delta_{\mathrm{tb}}(\lambda) = \lambda^2(\lambda + \sigma),$$
$$\sigma = 2r_2 + 5r_\mathrm{d} - g_o.$$

The conditions for the occurrence of the Takens–Bogdanov bifurcation in (12) are

$$g_o = \frac{r_2 + 4r_\mathrm{d}}{r_2^2 + 5r_2r_\mathrm{d} + 2r_\mathrm{d}^2},$$
$$0 = 1 + r_2^2 + 5r_2r_\mathrm{d} + 2r_\mathrm{d}^2 - g_o(2r_2 + 5r_\mathrm{d}).$$

System (12) can be described in the Jordan canonical form through the transformation ($y_i = T_{ij}x_j$)

$$T_{ij} = \begin{pmatrix} -\dfrac{2r_\mathrm{d}g_o}{r_2+4r_\mathrm{d}} & \dfrac{2r_\mathrm{d}\left(1 - g_o + \dfrac{g_o}{r_2+4r_\mathrm{d}}\right)}{r_2+4r_\mathrm{d}} & \dfrac{2r_\mathrm{d}(2r_2+5r_\mathrm{d})}{r_2+r_\mathrm{d}-g_o} \\ -g_o & 1-g_o & -2r_2-5r_\mathrm{d} \\ 1 & 1 & 1 \end{pmatrix}.$$

Using this transformation, the microgrid model becomes $\dot{x}_i = J_{ij}x_j + k_i f(x)$, where

$$J_{ij} = \begin{pmatrix} 0 & 1 & 0 \\ 0 & 0 & 0 \\ 0 & 0 & -\sigma \end{pmatrix}, \quad k_i = \begin{pmatrix} k_1 \\ k_2 \\ k_3 \end{pmatrix},$$

and

$$f(x) = \frac{(x_1 + x_2 + x_3)^2}{\mathcal{V}_o + x_1 + x_2 + x_3}.$$

The relation between the original microgrid parameters and the ones for the Takens–Bogdanov normal form are given by

$$k_1 = -\frac{g_o(2r_2 + 5r_\mathrm{d})\{g_o^2(r_2 + 4r_\mathrm{d} - 1) - g_o[2r_2^2 + 13r_2r_\mathrm{d} + r_\mathrm{d}(20r_\mathrm{d} + 3)] + 2r_2^2 + 13r_2r_\mathrm{d} + 20r_\mathrm{d}^2\}}{(g_o - 2r_2 - 5r_\mathrm{d})^2(g_o + r_2 + 4r_\mathrm{d})},$$

$$k_2 = \frac{g_o^2(r_2 + 4r_\mathrm{d})(2r_2 + 5r_\mathrm{d})}{(g_o - 2r_2 - 5r_\mathrm{d})(g_o + r_2 + 4r_\mathrm{d})},$$

$$k_3 = -\frac{g_o^3(g_o - r_2 - r_\mathrm{d})}{(g_o - 2r_2 - 5r_\mathrm{d})^2(g_o + r_2 + 4r_\mathrm{d})}.$$

Now, applying the center manifold theorem, i.e. $x_3 = h(x_1, x_2)$, and considering only the quadratic terms, the system becomes

$$\dot{x}_1 = x_2 + \frac{k_1}{\mathcal{V}_o}(x_1^2 + 2x_1x_2 + x_2^2) + \mathcal{O}(3), \quad (33)$$

$$\dot{x}_2 = \frac{k_2}{\mathcal{V}_o}(x_1^2 + 2x_1x_2 + x_2^2) + \mathcal{O}(3). \quad (34)$$

This pair of equations can be described in matricial form as $\dot{x}_i = J_{ij}x_j + k_i g(x)$, with $g(x) = x_1^2 + 2x_1x_2 + x_2^2$.

The normal form can be found by the following change of variables

$$x_i = w_i + h_i(w),$$

implying

$$\dot{x}_i = \left(\delta_{ij} + \frac{\partial h_i}{\partial w_j}\right)\dot{w}_j,$$

where δ_{ij} is the Kronecker delta. The dynamics of the new variable w_i is

$$\dot{w}_i = J_{ij}w_j + \left\{J_{ij}h_j - \frac{\partial h_i}{\partial w_j}J_{jk}w_k + k_i g(w)\right\} + \mathcal{O}(3), \quad (35)$$

with the mapping h_i given by

$$h_1 = a_{10}w_1^2 + a_{11}w_1w_2, \quad h_2 = b_{10}w_1^2 + b_{11}w_1w_2.$$

For the Takens normal form, the coefficients a_{ij} and b_{ij} are given by

$$a_{10} = \frac{2k_1 + k_2}{2\mathcal{V}_o}, \quad a_{11} = \frac{k_1}{\mathcal{V}_o},$$

$$b_{10} = \frac{k_2}{\mathcal{V}_o}, \quad b_{11} = b_{10},$$

resulting in

$$\begin{cases} \dot{w}_1 = w_2 + \dfrac{k_1 + k_2}{\mathcal{V}_o}w_1^2 + \mathcal{O}(3), \\ \dot{w}_2 = \dfrac{k_2}{\mathcal{V}_o}w_1^2 + \mathcal{O}(3). \end{cases} \quad (36)$$

In order to choose the Bogdanov normal form, the coefficients b_{ij} must be redefined to

$$b_{10} = -\frac{k_1}{\mathcal{V}_o}, \quad b_{11} = \frac{k_2}{\mathcal{V}_o}$$

and so the system becomes

$$\begin{cases} \dot{w}_1 = w_2 + \mathcal{O}(3), \\ \dot{w}_2 = \dfrac{k_2}{\mathcal{V}_o}w_1^2 + 2\dfrac{k_1 + k_2}{\mathcal{V}_o}w_1w_2 + \mathcal{O}(3). \end{cases} \quad (37)$$

System (36) [or System (37)] have a double zero eigenvalue.

4. Numerical Bifurcation Analysis

In this section, global bifurcations that may appear in (10) are studied by using numerical continuation

Table 1. DC microgrid parameters.

Parameter	Value	Normalized Value
R_1	45 mΩ	0.015
R_2	90 mΩ	0.03
L_1	450 μH	0.5
L_2	900 μH	1
C_o	100 μF	1
V_s	380 V	1
V_{th}	150 V	0.39474
$I_{\max}$	20 A	0.15789
P_{cps}	1 kW	0.02078

tools, such as the software AUTO [Doedel *et al.*, 1998]. The bifurcation diagrams are constructed by varying the CPL power (P_{cpl}) and capturing the dynamical behavior of the voltage v_o. The microgrid parameters are given in Table 1.

The numerical values for the Takens–Bogdanov (Sec. 3.3) are $r_{\text{d}} = 2.05299$, $g_o = 0.94319$ and $p_o = 0.235797$.

The bifurcation diagrams for different values of R_{d} using the software AUTO are shown in Figs. 9 to 11. Three different regions ①, ② and ③, characterized by the equilibria stability, are depicted in Fig. 9.

The following global bifurcations are identified in Figs. 9 to 11:

- Saddle-Node of Periodic Orbits (SNPO), where two periodic orbits (one unstable and the other stable) arise due to the piecewise load characteristic shown in Fig. 3.
- Boundary Equilibrium Bifurcation (BEB) [di Bernardo *et al.*, 2008; Pagano *et al.*, 2011], which occurs when the voltage (v_o) drops below V_{th} (see Fig. 3). This bifurcation behaves like a saddle-node of equilibrium points bifurcation (nonsmooth fold of equilibria).
- Homoclinic Connection (HC) occurs when the unstable limit cycle reaches the unstable equilibrium branch between SN and BEB, as can be seen in Fig. 10. Basically, the unstable limit cycle defines the attractive region of the upper stable equilibrium point and when the voltage drops outside this region it goes to the second stable equilibrium point determined by the BEB. When the HB reaches the SN a codimension-two point is detected corresponding to a Takens–Bogdanov bifurcation. A similar process happens when the SNPO reaches the BEB. Figure 8 can be redrawn, but now including the SNPO and the HC, as shown in Fig. 12. Notice that, when the SNPO disappears the HC appears.

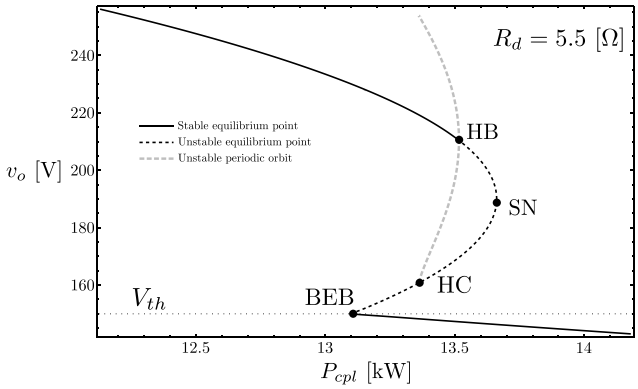

Fig. 10. Bifurcation diagram in (P_{cpl}, v_o)-plane for $R_{\text{d}} = 5.5$ [Ω].

The BEB occurs whenever $R_{\text{eq}}P_o = V_{\text{th}}(V_s - V_{\text{th}})$, this relation can be deduced based on the equilibria analysis in Sec. 2. When the voltage V_o is close to V_{th} there are three equilibrium points, one

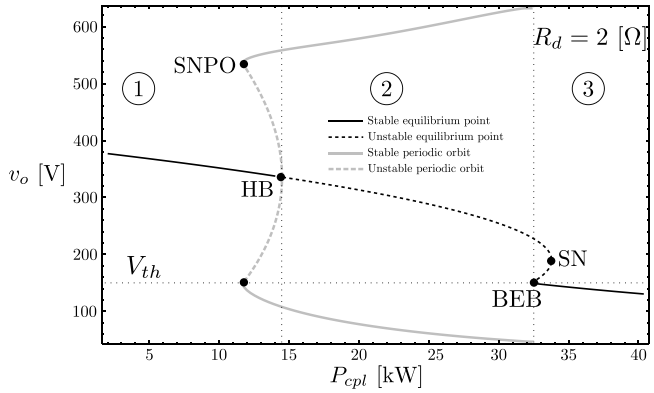

Fig. 9. Bifurcation diagram in (P_{cpl}, v_o)-plane for $R_{\text{d}} = 2$ [Ω].

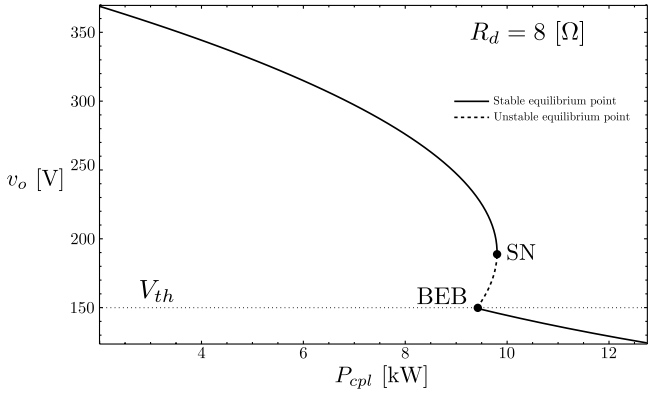

Fig. 11. Bifurcation diagram in (P_{cpl}, v_o)-plane for $R_{\text{d}} = 8$ [Ω].

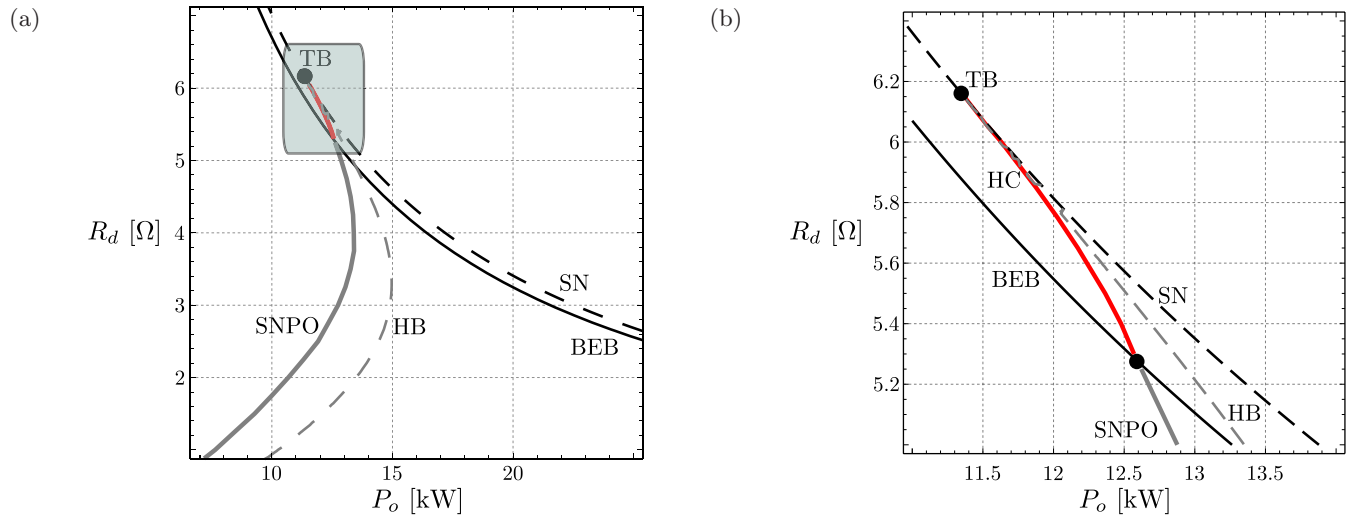

Fig. 12. Local and global bifurcation sets of codimension-two considering P_o and R_d as bifurcation parameters: (a) general picture of the bifurcations and (b) a zoom to show the Homoclinic Connection.

possible stable equilibrium, V_o^+ which is the solid black line in Fig. 7 (a Hopf bifurcation can make this branch unstable), one unstable, V_o^- which is the dashed black line and one stable equilibrium V_o that the BEB generates, the gray line. To show that this last equilibrium point is always stable, the linear part of (10) in region II (see Fig. 3) is investigated using the normalized equations:

$$A_{ij} = \begin{pmatrix} -(r_2 + 4r_\mathrm{d}) & 2r_\mathrm{d} & 0 \\ r_\mathrm{d} & -(r_2 + r_\mathrm{d}) & -1 \\ 0 & 1 & -\left(g_o + \dfrac{1}{r_\mathrm{th}}\right) \end{pmatrix}.$$

The load parameter is $g_o = p_\mathrm{cps}/\mathcal{V}_o^2$. Notice that the characteristic polynomial has positive coefficients, given by

$$\Delta(\lambda) = \lambda^3 + a_2\lambda^2 + a_1\lambda + a_0,$$

$$a_2 = 2r_2 + 5r_\mathrm{d} + \left(g_o + \frac{1}{r_\mathrm{th}}\right),$$

$$a_1 = 1 + r_\mathrm{eq}(r_2 + 4r_\mathrm{d}) + \left(g_o + \frac{1}{r_\mathrm{th}}\right)(2r_2 + 5r_\mathrm{d}),$$

$$a_0 = (r_2 + 4r_\mathrm{d})\left[1 + \left(g_o + \frac{1}{r_\mathrm{th}}\right) r_\mathrm{eq}\right]$$

and the condition $a_1 \geq a_0/a_2$ is always true, so the equilibrium point is asymptotically stable.

Bifurcation diagrams in Figs. 9 to 11 must be interpreted regarding the load power (P_cpl), which is a bifurcation parameter, as the true power of the system, but only in the nonlinear region of operation (region III in Fig. 3). In the other regions it is just a parameter related to the resistance, but it is not the power consumed by the load.

Although the focus of this paper is on the bifurcation analysis of system (1) considering the droop resistance, R_d, and the total power, P_o, as the main bifurcation parameters, other parameters of the reduced model can also affect the system dynamics. The line inductance (remember that $L_2 = 2L_1$) and the equivalent capacitor (C_o) can affect the Hopf bifurcation, as the power P_o is varied, but not the other bifurcations. To show the relation between these parameters and the Hopf bifurcation, codimension-two bifurcation sets are presented in Figs. 13 and 14 for (L_1, P_o) and for (C_o, P_o), respectively.

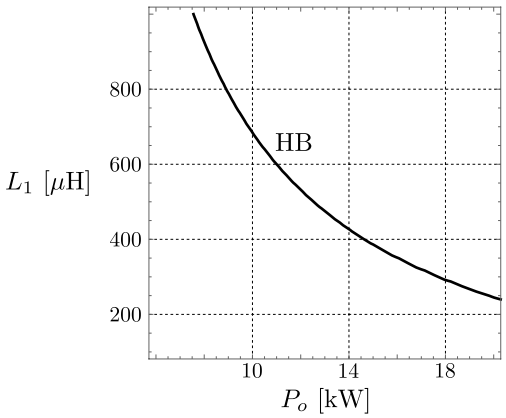

Fig. 13. Codimension-two bifurcation set showing the Hopf bifurcation, regarding P_o and L_1 as bifurcation parameters.

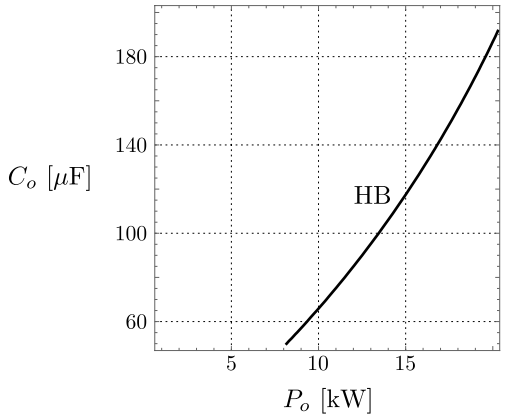

Fig. 14. Codimension-two bifurcation set showing the Hopf bifurcation, regarding P_o and C_o as bifurcation parameters.

In the former numerical analysis using AUTO, Eqs. (2) and (3) that are continuous but with discontinuous derivatives, are approximated to the following equations

$$i_{\rm cpl} = \frac{P_{\rm cpl}}{v_o}\left(0.5 + 0.5\tanh\frac{v_o - V_{\rm th}}{\epsilon}\right) + \frac{v_o}{R_{\rm th}}\left(0.5 - 0.5\tanh\frac{v_o - V_{\rm th}}{\epsilon}\right),$$

$$i_{\rm cps} = -\frac{P_{\rm cps}}{v_o}\left(0.5 + 0.5\tanh\frac{v_o - V_{\rm pv}}{\epsilon}\right) - I_{\max}\left(0.5 - 0.5\tanh\frac{v_o - V_{\rm pv}}{\epsilon}\right),$$

where ϵ must be a small value. Nonsmooth and smooth representations must have similar behavior as the parameter $\epsilon \to 0$.

5. Full Microgrid Model

The aim of this section is to compare numerically the dynamical behavior of the reduced model, considered in previous sections, with the full model of the microgrid system. The electrical circuits corresponding to the power converters of the studied microgrid are shown in Fig. 2 displaying its internal parameters.

The averaged equations of the AC-DC source, using the $dq0$ transform (the power invariant version), are given by

$$L_{\rm ac}\frac{di_{\rm d}}{dt} = \omega L_{\rm ac} i_q - u_{\rm d} v_1 + V_{\rm d},$$

$$L_{\rm ac}\frac{di_q}{dt} = -\omega L_{\rm ac} i_{\rm d} - u_q v_1,$$

$$C_1\frac{dv_1}{dt} = u_{\rm d} i_{\rm d} + u_q i_q - i_1,$$

with the control laws expressed as

$$u_{\rm d} = \frac{V_{\rm d} + \omega L_{\rm ac} i_q + K_1^i(i_{\rm d} - I_{\rm d,ref}) + K_2^i \xi_d}{v_1},$$

$$u_q = \frac{-\omega L_{\rm ac} i_{\rm d} + K_1^i i_q + K_2^i \xi_q}{v_1},$$

$$I_{\rm d,ref} = \frac{v_1}{V_{\rm d}}\{i_1 - K_1^v[v_1 - (V_s - R_{\rm d} i_1)] - K_2^v \xi_1\}$$

and the following terms being the output of the integral action presented in the control laws:

$$\frac{d\xi_d}{dt} = i_{\rm d} - I_{\rm d,ref},$$

$$\frac{d\xi_q}{dt} = i_q,$$

$$\frac{d\xi_1}{dt} = v_1 - (V_s - R_{\rm d} i_1).$$

The voltage v_1 is the AC-DC source output voltage, the voltage $V_{\rm d}$ is the input direct-axis AC voltage, and $\{i_{\rm d},\ i_q\}$ are the {direct, quadrature}-axes AC currents, all properly transformed to DC signals. The controller gains are K_j^i for the current loop and K_j^v for the voltage loop, with $j \in \{1, 2\}$.

For the DC-DC source, the equations are

$$L_{\rm bat}\frac{di_{\rm bat}}{dt} = -v_2(1 - u_{\rm bat}) + V_{\rm bat},$$

$$C_2\frac{dv_2}{dt} = i_{\rm bat}(1 - u_{\rm bat}) - (i_2 - i_1),$$

with the following control laws

$$u_{\rm bat} = 1 - \frac{V_{\rm bat} + K_p^{\rm bat}(i_{\rm bat} - I_{\rm bat,ref})}{v_2},$$

$$I_{\rm bat,ref} = \frac{v_2}{V_{\rm bat}}\{(i_2 - i_1) - K_1^v[v_2 - (V_s - R_{\rm d}(i_2 - i_1))] - K_2^v \xi_{\rm bat}\}$$

and

$$\frac{d\xi_{\rm bat}}{dt} = v_2 - (V_s - R_{\rm d}(i_2 - i_1)).$$

The voltage v_2 is the DC-DC source output voltage, the voltage $V_{\rm bat}$ is the battery voltage, and the controller gains are $K_p^{\rm bat}$ for the current control loop and K_j^v for the voltage control loop.

Table 2. AC-DC and DC-DC source parameters.

Parameter	Value	Parameter	Value
L_{ac}	750 μH	L_{bat}	1 mH
C_1	500 μF	C_2	500 μF
V_{d}	122.475 V	V_{bat}	100 V
K_1^i	1.999	K_p^{bat}	1.25664
K_2^i	2664.79	K_1^v	0.0444221
ω	377 rad/s	K_2^v	1.97392

The equations of the load model corresponding to a controlled power converter with a resistive load are given by

$$L_l \frac{di_{\text{cpl}}}{dt} = v_o(-K_0 i_{\text{cpl}} - K_1 v_{\text{cpl}} - K_2 \xi_{\text{cpl}}) - v_{\text{cpl}},$$

$$C_l \frac{dv_{\text{cpl}}}{dt} = i_{\text{cpl}} - \frac{v_{\text{cpl}}}{R_o},$$

$$\frac{d\xi_{\text{cpl}}}{dt} = v_{\text{cpl}} - V_{\text{th}}.$$

Notice that, the control law used is the usual state feedback control with an integral action (ξ_{cpl}), and the gains of the controller are K_0, K_1 and K_2. The load input voltage is v_o, where the output voltage is v_{cpl}. The inductor current is i_{cpl}, and R_o is a resistive load. The reference signal for the load is V_{th}, which is defined in Table 1.

The PV system equations are given by

$$C_{\text{pv}} \frac{dv_{\text{pv}}}{dt} = i_{\text{pv}}(v_{\text{pv}}) - i_{\text{Lp}},$$

$$L_{\text{pv}} \frac{di_{\text{Lp}}}{dt} = v_{\text{pv}} - (1 - u_{\text{pv}})v_o,$$

where v_{pv} is the voltage on the capacitor in the input terminals of the PV panel, i_{pv} is the PV panel current and i_{Lp} is the inductor current. The control law for the PV system is a simple static nonlinear equation, given by

$$u_{\text{pv}} = 1 - \frac{v_{\text{pv}} + K_{\text{pv}}(i_{\text{Lp}} - I_{\text{mppt}})}{v_o},$$

with I_{mppt} being the reference signal generated by the Maximum Power Point Tracking (MPPT)

Table 3. CPS and CPL parameters.

Parameter	Value	Parameter	Value
L_l	1 mH	L_{pv}	1 mH
C_l	100 μF	C_{pv}	10 μF
K_0	0.145968	K_{pv}	6
K_1	0.0191522	K_2	156.663

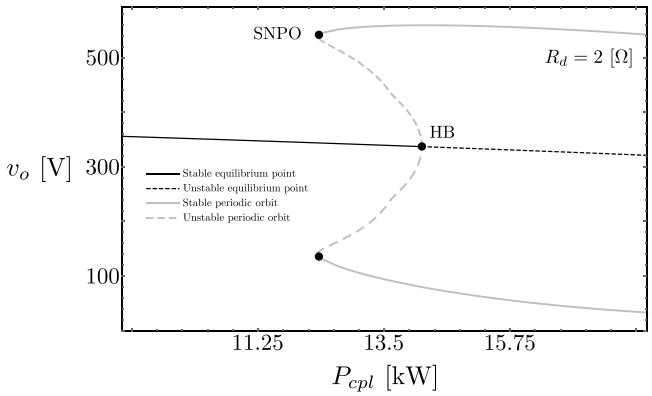

Fig. 15. Bifurcation diagram in (P_{cpl}, v_o)-plane for $R_{\text{d}} = 2$ [Ω], valid for the full microgrid model in the power range from 9 [kW] to 18 [kW] (cf. Fig. 9).

system, and K_{pv} the controller gain. Note that Fig. 2 shows the line impedance between the PV and the power converter, but this impedance is neglected for the full model.

The numerical values used for the AC-DC source and DC-DC source parameters are shown in Table 2, and for the CPS and CPL are shown in Table 3.

In order to show that the reduced model can capture the essential qualitatively dynamic behavior of the microgrid, the bifurcation diagram for the full model is shown in Fig. 15. Notice that HB and SNPO points are close for both models (cf. Fig. 9).

6. Shortcomings of the Proposed Reduced Model

One of the problems with the reduced model is the parameter R_{d}, because this resistance is not linked to a physical element. It is not a resistor but instead it is an effect due to the voltage source control system, which has some dynamics that are not captured by the proposed model. The advantage of this approach compared to a physical resistor is that it does not dissipate any energy. The Hopf bifurcation is affected by this dynamic and it is expected that the limit cycle occurs for a lower value of the power drawn by the load. To compensate for the lack of dynamics linked to R_{d}, the load is modeled as CPL, which is a worst-case scenario modeling. If the load has fast dynamics, the error between the proposed reduced model and the full microgrid model will be minimum, but notice that several problems can occur if one wants to use a partial reduced model, for instance, using a complete model for the sources

but still using a CPL model for the loads. This approach will generate a considerably large error.

Another issue where the reduced model can exhibit problems is the presence of saturation in the voltage source control loop. It is not possible to keep increasing the droop gain ($R_{\rm d}$) without avoiding the possibility of saturating the control loop, and when this happens, the occurrence of a Hopf bifurcation that is not linked to the one presented along this paper is expected. The SNPO bifurcation is highly dependent on the overall system dynamics, and with minor changes in the gains of the source controller, it is possible to change its value and even to shrink the region between the SNPO and the Hopf bifurcation, so that the original subcritical Hopf bifurcation can become almost a supercritical one.

In order to show more in depth the effects of the disregarded dynamics, bifurcation diagrams corresponding to the full microgrid model and for the parameters K_1^v and K_2^v are presented in Figs. 16 and 17. For lower values of K_1^v, the reduced model fits well, but by increasing its value, a subcritical Hopf bifurcation will appear (this is a new Hopf bifurcation, not linked to the one shown in Fig. 15). Note that as the gain is increased, the stable limit cycle suffers another bifurcation, a Hopf of Periodic Orbit (HPO), which is a Neimark–Sacker bifurcation when the Poincaré map is applied to the periodic orbit. The second parameter (K_2^v) presents a similar diagram, but now the Hopf bifurcation is of a supercritical type. As these parameters do not appear in the proposed model, they must be in the stable range of the equilibrium point, so the reduced model can capture the microgrid dynamics properly.

The codimension-two bifurcation set showing the Hopf bifurcation (cf. Fig. 15) for K_1^i and $K_p^{\rm bat}$, the current control loop proportional gain

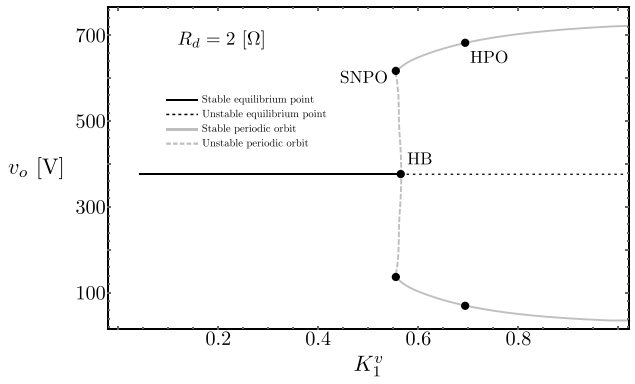

Fig. 16. Bifurcation diagram in (K_1^v, v_o)-plane for $R_{\rm d} = 2$ [Ω].

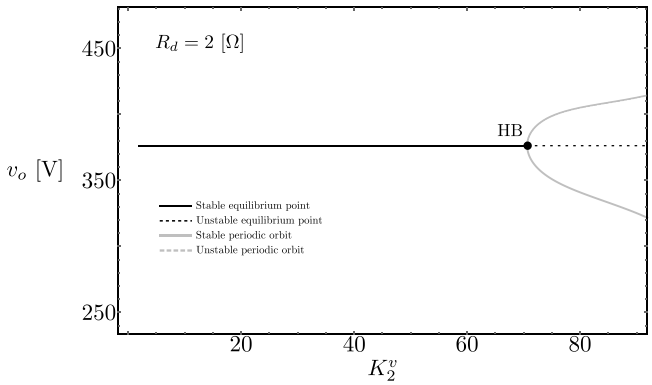

Fig. 17. Bifurcation diagram in (K_2^v, v_o)-plane for $R_{\rm d} = 2$ [Ω].

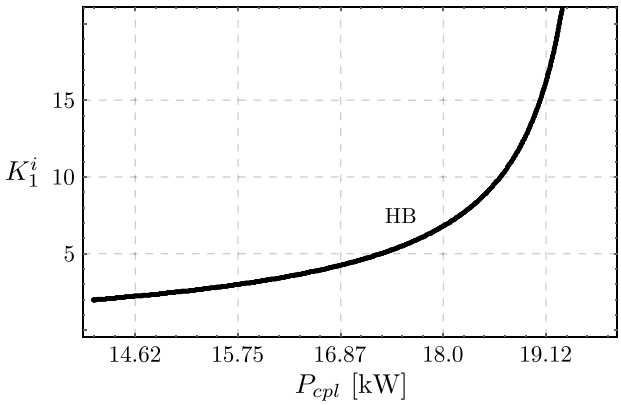

Fig. 18. Codimension-two bifurcation set showing the Hopf bifurcation, regarding $P_{\rm cpl}$ and K_1^i as the bifurcation parameters.

of the AC-DC source and DC-DC source respectively, can be seen in Figs. 18 and 19. These results show a strong interaction between the sources of the current control loop parameters and the Hopf bifurcation.

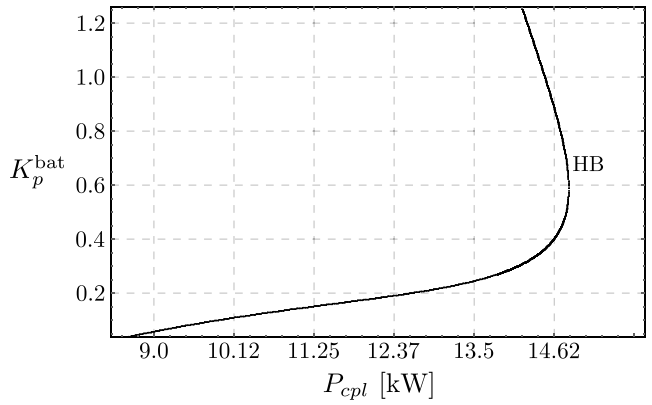

Fig. 19. Codimension-two bifurcation set showing the Hopf bifurcation, regarding $P_{\rm cpl}$ and $K_p^{\rm bat}$ as the bifurcation parameters.

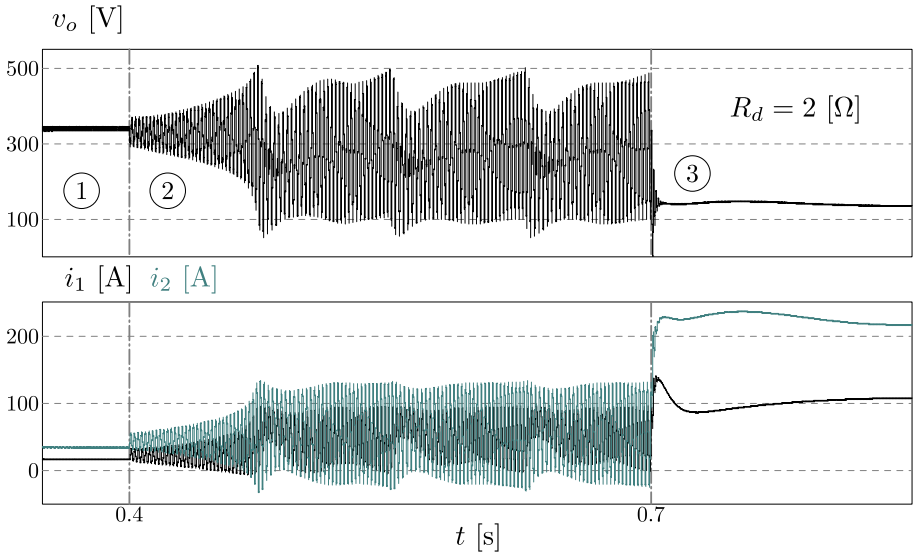

Fig. 20. Simulation of the DC microgrid showing the voltage v_o and the currents i_1 and i_2 in the main three operating regions (see the encircled numbers 1, 2 and 3 in Fig. 9) valid for $R_{\mathrm{d}} = 2\ \Omega$.

7. Simulation Results

The aim of this section is to validate the bifurcation analysis done in the previous sections through simulation results obtained from the commercial package PSIM. It is noteworthy to remark that these results were obtained considering the whole model of the proposed DC microgrid. Note that there are three models presented in this paper: (a) the reduced model; (b) full model, used in Sec. 5, which is based on the average model for the power converters; (c) instantaneous model used to obtain the numerical PSIM simulations, which is based on switching models for all the power converters with discrete controllers. Also, it must be stressed that the simulation results are qualitatively equivalent with the ones obtained by applied numerical continuation methods on the reduced microgrid model.

7.1. *Time-domain response analysis*

Time-domain charts corresponding to the voltage $v_o(t)$ and the currents $i_1(t)$, $i_2(t)$ for different load power steps are depicted in Fig. 20. The numbers ①, ②, ③ in Fig. 20 denote the different regions characterized in Fig. 9.

As shown in Fig. 20, until $t = 0.4$ [s], the system equilibrium point is stable (region ①) with $P_{\mathrm{cpl}} = 12.85$ [kW]. After a step in the load power ($P_{\mathrm{cpl}} = 15$ [kW]) the equilibrium point becomes unstable and the voltage v_o begins to oscillate (region ②). At $t = 0.7$ [s], a large step in the load power is applied ($P_{\mathrm{cpl}} = 37.5$ [kW]), and a new stable equilibrium point appears due to the BEB (region ③). Clearly, region ① in Fig. 20 is the stable operating region and the other cases correspond to undesirable operating regimens that must be avoided using adequate protection mechanisms. The shape of the limit cycle can be seen in Fig. 21, which shows that the periodic oscillation contains the fundamental component and other harmonic frequencies.

In order to show the SNPO bifurcation (Fig. 22), a step in the load power at $t = 0.4$ [s] is applied so that the system enters the region where it should oscillate. In the sequence, at $t = 0.5$ [s], the power is reduced to a level where the equilibrium point should be stable. Observing with care, one will notice that the Hopf bifurcation in Fig. 20 happens

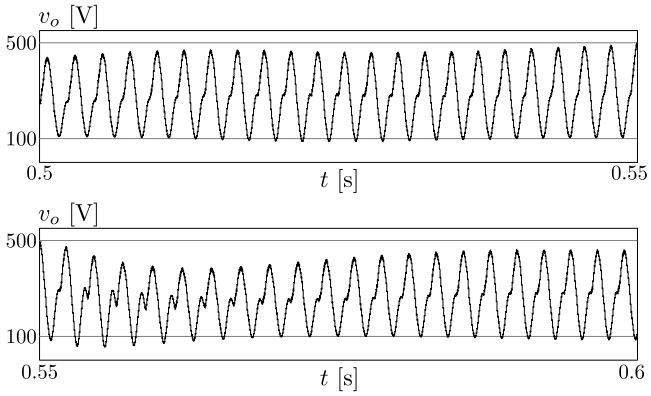

Fig. 21. The limit cycle waveform corresponding to the simulation shown in Fig. 20, captured from $t = 0.5$ [s] to 0.6 [s], for $R_{\mathrm{d}} = 2$ [Ω].

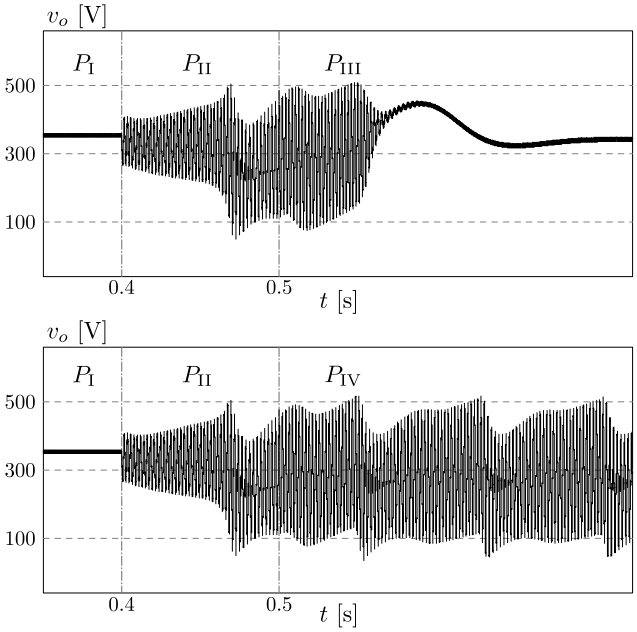

Fig. 22. Simulation showing the SNPO bifurcation for steps in the CPL power ($P_{\mathrm{I}} = 9$ [kW], $P_{\mathrm{II}} = 15$ [kW], $P_{\mathrm{III}} = 12.5$ [kW], $P_{\mathrm{IV}} = 13.2$ [kW]), valid for $R_{\mathrm{d}} = 2$ [Ω].

when the load power reaches $P_{\mathrm{cpl}} = 15$ [kW], but in Fig. 22, when the system is already oscillating, one must go below $P_{\mathrm{cpl}} = 12.5$ [kW] to stop the oscillations. The region between $P_{\mathrm{cpl}} = 12.5$ [kW] and $P_{\mathrm{cpl}} = 15$ [kW] have two limit cycles, an inner unstable and an outer stable, which was foreseen by the reduced model. This is a parametric hysteresis, as the value where the voltage starts to oscillate when the equilibrium point is stable is different from the value when the system is already oscillating and the power is decreased so the equilibrium point is stable.

The case where the droop resistance is big enough so no Hopf bifurcation appears ($R_{\mathrm{d}} = 8$ [Ω]) is shown in Fig. 23. At $t = 0.3$ [s], the CPL power suffers a step from $P_{\mathrm{cpl}} = 4.5$ [kW] to $P_{\mathrm{cpl}} = 9$ [kW], and at $t = 0.5$ [s] another step of $P_{\mathrm{cpl}} = 10$ [kW] is applied, where the system undergoes a BEB.

The reduced model indicates that the presence of the PV source makes the microgrid more stable. The effects of the PV source in the voltage v_o and currents i_1 and i_2, as the PV power is varied can be seen in Fig. 24, for the case when the CPL power is very low. When the CPL power is close to the Hopf bifurcation, any variation on the PV power can make the system oscillate, as shown in Fig. 25, where a step change in the CPS power (P_{cps}) was applied at $t = 0.5$ [s]. The oscillatory behavior starting close to $t = 0.7$ [s] is due to the instability generated by the Hopf bifurcation, and no other step changes were made for this simulation. Close to $t = 0.7$ [s] the dc-dc power converter duty cycle (u_{bat} waveform in Fig. 25) saturates only on the upper value, but not on the lower value. This saturation leads to an asymmetrical bus voltage waveform which decreases its average value, but not the average voltage on the CPL, and this causes an increase in the average CPL power.

The AC currents of the AC-DC source can be seen in Fig. 26 for the three main operating regions (cf. Fig. 9), which shows that the control can make

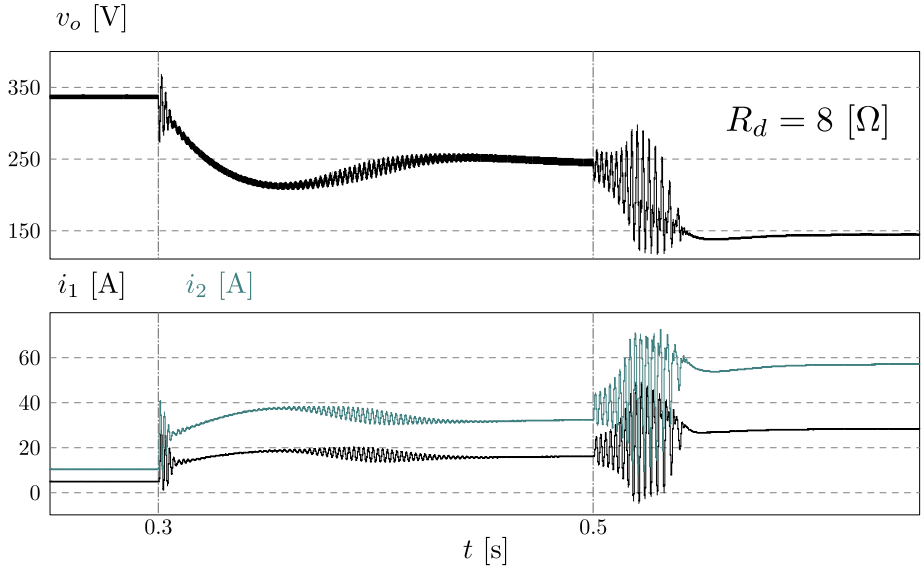

Fig. 23. Simulation of the whole DC microgrid showing the voltage v_o and the currents i_1 and i_2 valid for $R_{\mathrm{d}} = 8$ [Ω].

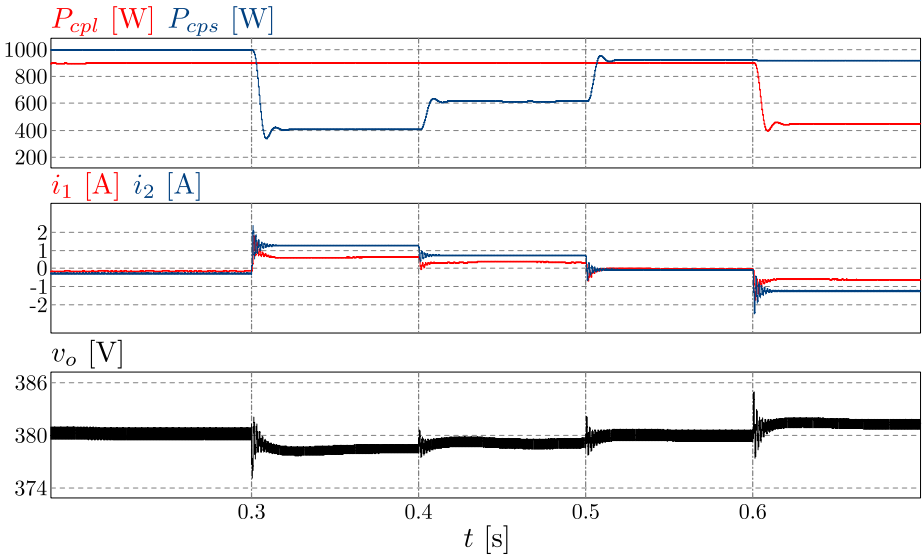

Fig. 24. Simulation of steps in the PV power source (CPS) showing the voltage v_o, the powers P_{cpl} and P_{cps}, and the currents i_1 and i_2, valid for $R_{\text{d}} = 2$ [Ω].

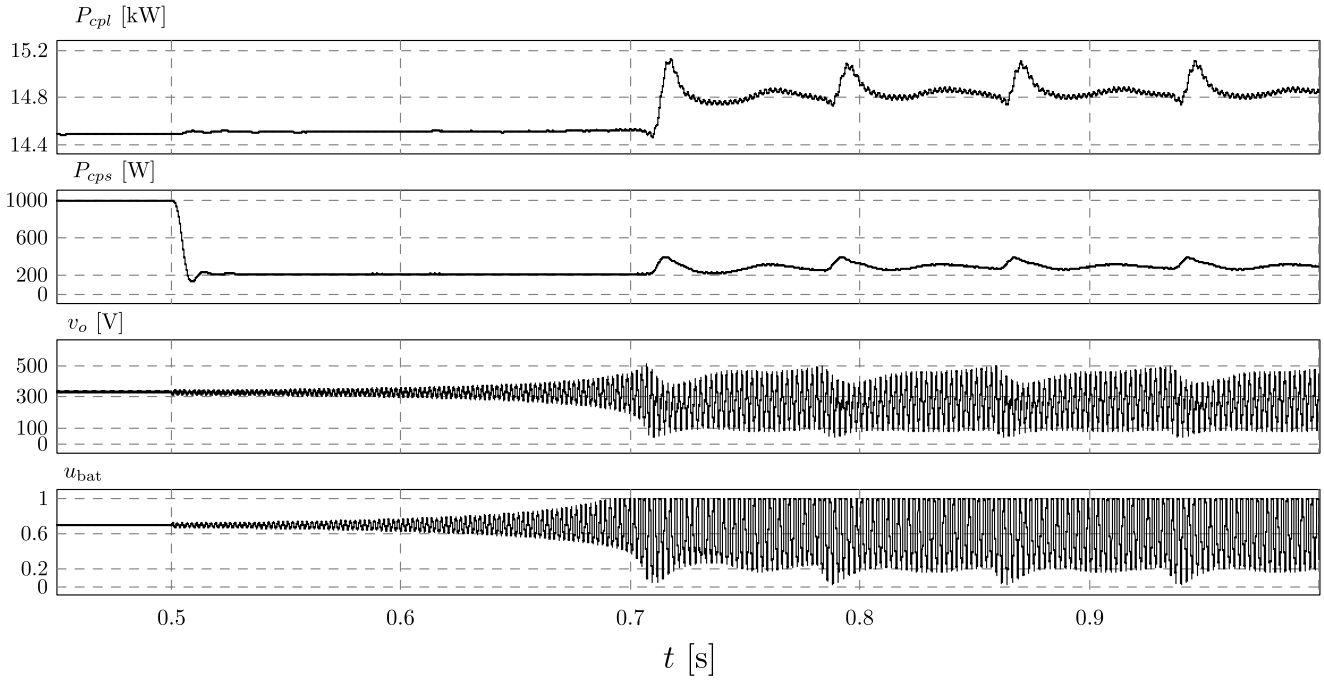

Fig. 25. Simulation of a step in the PV power source (P_{cps}) at $t = 0.5$ [s], showing the bus voltage v_o, the DC-DC power converter duty cycle u_{bat}, and the powers P_{cpl} and P_{cps}, valid for $R_{\text{d}} = 2$ [Ω].

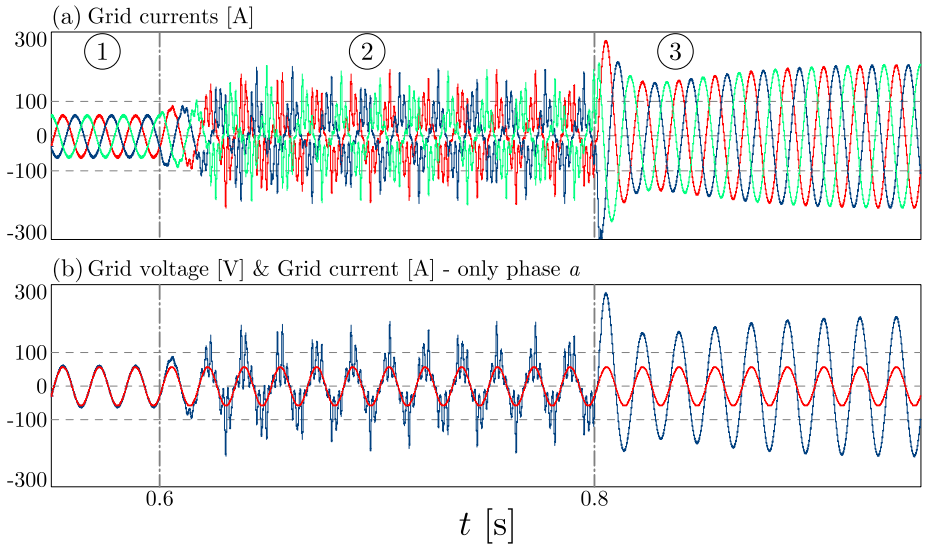

Fig. 26. Simulation of the whole DC microgrid showing (a) the three-phase AC grid currents from the AC-DC voltage source and (b) AC grid voltage and current for only phase a.

the power factor almost unitary when the equilibrium point is stable.

As a practical rule the value of $R_{\rm d}$ can be chosen between 2 [Ω] and 3 [Ω]. Greater values, although can increase the power range where the equilibrium point is stable, can decrease the voltage V_o away from the desired voltage V_s (380 [V] in the microgrid under study).

8. Conclusion

This paper addresses the effects of the droop control resistance ($R_{\rm d}$) on the dynamical behavior of a DC microgrid. A case study was analyzed using standard local bifurcation analysis and numerical continuation methods. The main contribution of this work is a codimension-two bifurcation analysis of a small DC microgrid under droop control, considering the droop control gain and the power processed by the load as bifurcation parameters. In this sense, a codimension-two bifurcation set allows us to understand the complex dynamical behavior that this DC microgrid can exhibit and, at the same time, leads to practical rules for choosing the droop gain ($R_{\rm d}$) in order to achieve a robust droop control design for a desired power range. Furthermore, the existence of local bifurcations of equilibrium points was proved from a theoretical framework using a low order model to characterize the complex dynamical behavior due to the interaction between sources, loads and the impedance transmission lines. The proposed reduced model captures qualitatively the essence of the microgrid dynamics as shown by numerical simulations.

Acknowledgments

This work was developed within the R&D Program framework of Tractebel Energia S.A. according to the Brazilian Electrical Energy National Agency (ANEEL) regulation.

References

Boroyevich, D., Cvetkovic, I., Burgos, R. & Dong, D. [2013] "Intergrid: A future electronic energy network?" *IEEE Trans. Emerg. Sel. Topics Power Electron.* **1**, 127–138.

di Bernardo, M., Pagano, D. J. & Ponce, E. [2008] "Non hyperbolic boundary equilibrium bifurcations in planar Filippov systems: A case study approach," *Int. J. Bifurcation and Chaos* **8**, 1377–1392.

Doedel, E. J., Champneys, A. R., Fairgrieve, T. F., Kuznetsov, Y. A., Sandstede, B. & Wang, X. [1998] *Auto 97*: *Continuation and Bifurcation Software for Ordinary Differential Equations* (*with Homcont*).

Dragicevic, T., Guerrero, J. M., Vasquez, J. C. & Skrlec, D. [2014] "Supervisory control of an adaptive-droop regulated DC microgrid with battery management capability," *IEEE Trans. Power Electron.* **29**, 695–706.

Du, W., Zhang, J., Zhang, Y. & Qian, Z. [2013] "Stability criterion for cascaded system with constant power load," *IEEE Trans. Power Electron.* **28**, 1843–1851.

Gavagsaz-Ghoachani, R., Martin, J.-P., Pierfederici, S., Nahid-Mobarakeh, B. & Davat, B. [2013] "DC power

networks with very low capacitances for transportation systems: Dynamic behavior analysis," *IEEE Trans. Power Electron.* **28**, 5865–5877.

Guckenheimer, J. & Holmes, P. [1983] *Nonlinear Oscillations, Dynamical Systems, and Bifurcations of Vector Fields* (Springer).

Guerrero, J. M., Vasquez, J. C., Matas, J., de Vicua, L. G. & Castilla, M. [2011] "Hierarchical control of droop-controlled AC and DC microgrids — A general approach toward standardization," *IEEE Trans. Ind. Electron.* **58**, 158–172.

Kuznetsov, Y. [2004] *Elements of Applied Bifurcation Theory*, 3rd edition (Springer).

Lu, X., Guerrero, J. M., Sun, K. & Vasquez, J. C. [2014] "An improved droop control method for DC microgrids based on low bandwidth communication with DC bus voltage restoration and enhanced current sharing accuracy," *IEEE Trans. Power Electron.* **29**, 1800–1812.

Magne, P., Marx, D., Nahid-Mobarakeh, B. & Pierfederici, S. [2012] "Large-signal stabilization of a DC-link supplying a constant power load using a virtual capacitor: Impact on the domain of attraction," *IEEE Trans. Ind. Appl.* **48**, 878–887.

Onwuchekwa, C. & Kwasinski, A. [2010] "Analysis of boundary control for buck converters with instantaneous constant-power loads," *IEEE Trans. Power Electron.* **25**, 2018–2032.

Pagano, D. J., Ponce, E. & Torres, F. [2011] "On double boundary equilibrium bifurcations in piecewise smooth planar systems," *Qual. Th. Dyn. Syst.* **10**, 277–301.

Planas, E., de Muro, A. G., Andreu, J., Kortabarria, I. & de Alegría, I. M. [2013] "General aspects, hierarchical controls and droop methods in microgrids: A review," *Renew. Sustain. Energy Rev.* **17**, 147–159.

Radwan, A. A. A. & Mohamed, Y. A.-R. I. [2012] "Linear active stabilization of converter-dominated DC microgrids," *IEEE Trans. Smart Grid* **3**, 203–216.

Tahim, A. P. N., Pagano, D. J., Lenz, E. & Stramosk, V. [2015] "Modeling and stability analysis of islanded DC microgrids under droop control," *IEEE Trans. Power Electron.* **30**, 4597–4607.

Xiong, X., Tse, C. K. & Ruan, X. [2013a] "Bifurcation analysis of standalone photovoltaic-battery hybrid power system," *IEEE Trans. Circuits Syst.-I: Reg. Papers* **60**, 1354–1365.

Xiong, X., Tse, C. K. & Ruan, X. [2013b] "Smooth and nonsmooth bifurcations in multi-structure multi-operating-mode hybrid power systems," *Int. J. Bifurcation and Chaos* **23**, 1350094-1–12.

Zhang, F. & Yan, Y. [2011] "Start-up process and step response of a DC-DC converter loaded by constant power loads," *IEEE Trans. Ind. Electron.* **58**, 298–304.